
Supplementary information

Magnetic sensitivity of cryptochrome 4 from a migratory songbird

In the format provided by the
authors and unedited

Magnetic sensitivity of cryptochrome 4 from a migratory songbird

Jingjing Xu, Lauren E. Jarocho, Tilo Zollitsch, Marcin Konowalczyk, Kevin B. Henbest, Sabine Richert, Matthew J. Golesworthy, Jessica Schmidt, Victoire Déjean, Daniel J. C. Sowood, Marco Bassetto, Jiate Luo, Jessica R. Walton, Jessica Fleming, Yujing Wei, Tommy L. Pitcher, Gabriel Moise, Maïke Herrmann, Hang Yin, Haijia Wu, Rabea Bartölke, Stefanie J. Käsehagen, Simon Horst, Glen Dautaj, Patrick D. F. Murton, Angela S. Gehrckens, Yogarany Chelliah, Joseph S. Takahashi, Karl-Wilhelm Koch, Stefan Weber, Ilia A. Solov'yov, Can Xie, Stuart R. Mackenzie, Christiane R. Timmel, Henrik Mouritsen, P. J. Hore

Methods and Supplementary Information

Table of Contents

	page
Methods	
Statistics and reproducibility	3
Protein expression and purification	7
Key resource table for protein expression and purification	10
Picosecond transient absorption (TA)	11
Cavity ring-down spectroscopy (CRDS)	11
Broadband cavity-enhanced absorption spectroscopy (BBCEAS)	12
Continuous photoreduction	14
Re-oxidation experiments	14
Electron paramagnetic resonance (EPR)	14
Key resource table for spectroscopic experiments	16
Spin dynamics calculations	17
Molecular dynamics simulations of <i>ErCry4</i>	18
Quantum chemical calculations of FAD, FAD ^{•-} , TrpH, and TrpH ^{•+} self-energies	19
Electron transfer rate constants	20
Code availability	21
Additional information	21
Supplementary Information section	
UV-visible spectra of <i>ErCry4</i> WT and W _X F mutants	22
Transient absorption kinetics and spectra of <i>ErCry4</i> WT and mutants	23
Comparison of magnetic field effects for <i>ErCry4</i> variants	24
Rate constants of the reactions of the RP _C /RP _D composite radical pair	25
Simulation of OOP-ESEEM data	27
Spectra of ⁵ FAD* and ¹ FAD*	29
Choice of pH 8 for spectroscopic measurements at 5 °C	30
<i>ErCry4</i> stability in MD simulations	31
Edge-to-edge distances	32
Centre-to-centre distances	34
Electron transfer rate constants	36
Hydrogen bonding network	40
Radical pair kinetics from transient absorption measurements	41

Incorporation of FAD in <i>ErCry4</i>	42
Photoreduction of <i>ErCry4</i> W _D F	43
Re-oxidation kinetics of <i>ErCry4</i> WT	44
Magnetic field effects without added ferricyanide	51
References	53

Methods

Statistics and reproducibility

Fig. 1 | European robin cryptochrome 4: purification, electron transfer pathway, and photoreduction.

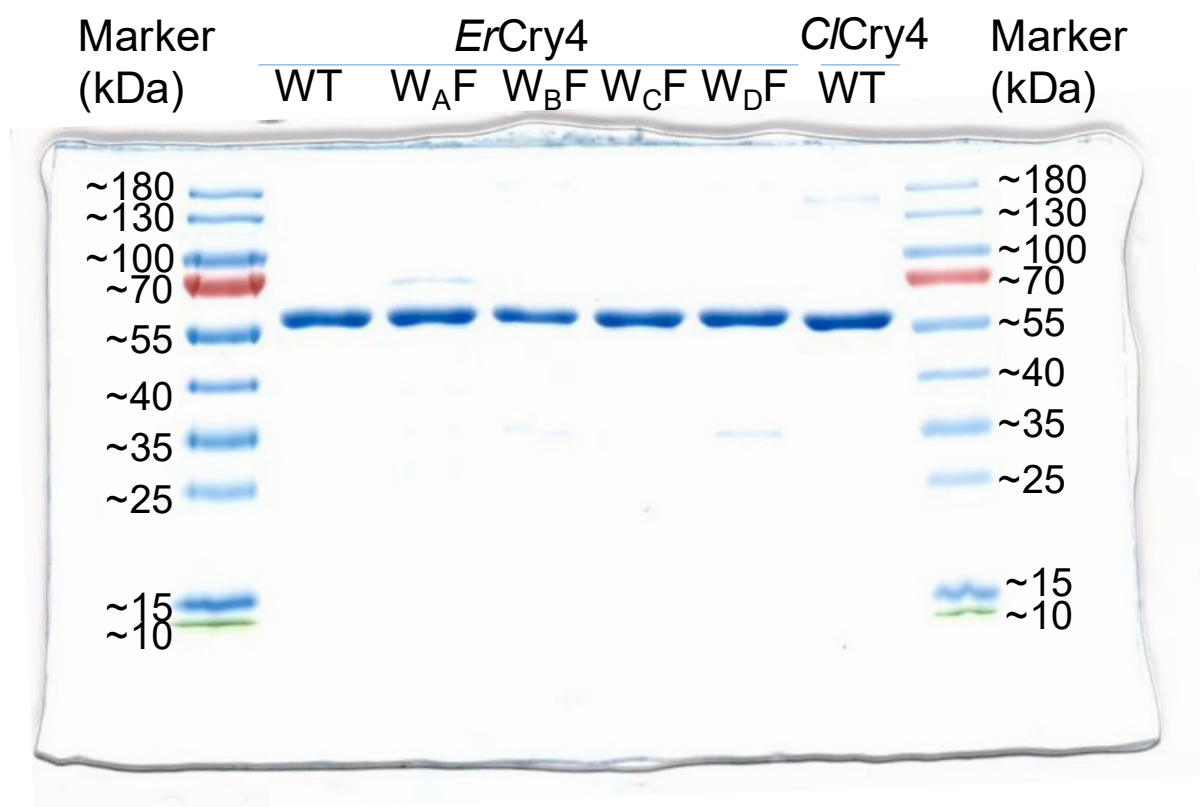
a, Experimental conditions: pH 8.0 Tris buffer.

Chromatography data very similar to Fig. 1a exist for every individual Cry4 protein purification batch (127 independent batches in total). However, in some cases, the Cry4 peak was smaller than in Fig. 1a so that more *E. coli* culture flasks were needed to produce one pure protein sample batch for measurements. This did not, however, affect the purity of the isolated Cry4, only the yield of the collected Cry4 per culture flask. For the present study, a total of ca. 1480 flasks containing ca. 0.7 L *E. coli* cell culture were used to isolate protein samples (*ErCry4* WT: 58 repeats, 188.2 mg; *ErCry4* W_AF: 4 repeats, 5.3mg; *ErCry4* W_BF: 4 repeats, 4.0 mg; *ErCry4* W_CF: 5 repeats, 8.7 mg; *ErCry4* W_DF: 32 repeats, 135.4 mg; *ClCry4* WT: 9 repeats, 90.3 mg; *GgCry4* WT: 15 repeats, 48.6 mg).

Summary of protein samples

Protein	Independent repeat/batch	<i>E. coli</i> cell culture (flasks)	Anion exchange chromatography runs on Äkta	Total amount / mg
<i>ErCry4</i> WT	58	729	79	188.2
<i>ErCry4</i> W395F (W _A F)	4	36	4	5.3
<i>ErCry4</i> W372F (W _B F)	4	36	4	4.0
<i>ErCry4</i> W318F (W _C F)	5	60	5	8.7
<i>ErCry4</i> W369F (W _D F)	32	435	54	135.4
<i>ClCry4</i> WT	9	69	15	90.3
<i>GgCry4</i> WT	15	114	17	48.6

b , The purity of every sample batch was checked (by SDS-PAGE with Coomassie blue staining) before shipment from the production lab in Oldenburg to the measurement location in Oxford. In our daily work, we ran gels for each batch of protein separately (two gels for each of the ca. 178 ÄKTA purification runs required to produce the samples for this paper). All samples sent to Oxford had a purity very similar to the blot in Fig. 1b. All *ErCry4* proteins (WT and mutants) and *C/Cry4* WT were run together on a single blot for Fig. 1b. The blot has not been cropped, cut, merged or modified in any way. The original is shown below.



d, Experimental conditions: 30 μ M protein samples in 20 mM Tris buffer, pH 8.0, with 20% glycerol at 5 $^{\circ}$ C. 5 mM dithiothreitol was added as an external electron donor.

Data shown for a single protein sample. Reproducibility was checked with three independently produced samples with comparable results. See Methods (Continuous photoreduction) for further details.

e, WT data are for a single protein sample. Reproducibility was checked with two independently produced samples with comparable results. $W_D F$ data are for a single protein sample. Reproducibility was checked with two independently produced samples with comparable results. See Methods (Continuous photoreduction) for further details.

f, The illumination at 450 nm with intensity $260 \mu\text{mol m}^{-2} \text{s}^{-1}$ produced a steady state with approximately equal amounts of the FAD^{ox} and FADH^{\bullet} forms of the protein. Experimental conditions: 35 μ M protein in 20 mM Tris buffer, pH 8.0, 200 mM NaCl, with 20% glycerol at 20 $^{\circ}$ C.

WT data are for a single protein sample. Reproducibility was checked with two independently produced samples with comparable results. $W_D F$ data are for a single protein sample. Reproducibility was checked with two independently produced samples with comparable results. See Methods (Re-oxidation experiments) for further details.

Fig. 2 | Magnetic field effects on the yields of photo-induced radicals in Cry4s.

a and b, Experimental conditions: 60–70 μM protein in 10 mM Tris buffer with 20% glycerol and 5 mM $\text{K}_3\text{Fe}(\text{CN})_3$ at 5 °C. The error bars for the pH 8 measurement in **a** are larger because less signal averaging was performed than for the other three (which were all at pH ≈ 7). The parameter $B_{1/2}$ is the magnetic field that produces 50% of the effect at high field. The data are presented as mean values \pm SEM (standard error of the mean) and the lines are Lorentzian fits to the data. See Methods (Cavity ring-down spectroscopy) for further details.

a, The *ErCry4* pH 7 data are averages of 50 measurements on a single protein sample. Reproducibility was checked with two independently produced samples with comparable results.

The *ErCry4* pH 8 data are averages of 20 measurements on a single protein sample. Reproducibility was checked with an independently produced sample with comparable results.

b, The *AtCry1* data are averages of 50 measurements on a single protein sample. Reproducibility was checked with an independently produced sample with comparable results.

The *ErCry4* W_dF data are averages of 50 measurements on a single protein sample. Reproducibility was checked with an independently produced sample with comparable results.

c, Experimental conditions: 10 μM protein in 50 mM Tris buffer, pH 8.0, with 20% glycerol at 5 °C. 5 mM $\text{K}_3\text{Fe}(\text{CN})_6$ was added to promote sample re-oxidation after photoreduction. Using the values of $\Delta\Delta A$ and the extinction coefficient of Trp^\bullet it is found that the magnetic field reduces the yield of this radical by ca. 5 nM for *ErCry4* but only ca. 200 pM for *C/Cry4* and *GgCry4*.

The *ErCry4*, *GgCry4* and *C/Cry4* spectra are averages of 10, 15 and 17 measurements, respectively, on a single sample of each protein. In each case reproducibility was checked with an independently produced sample with comparable results. See Methods (Broadband cavity-enhanced absorption spectroscopy) for further details.

d, Experimental conditions: same as for **a** except pH = 8.0. The data are presented as mean values \pm SEM. The lines are smooth curves to guide the eye.

Each data point shown results from n measurements on the same protein sample, where $n = 176 \pm 12$ for *ErCry4*, $n = 48 \pm 13$ for *GgCry4*, $n = 146 \pm 2$ for *C/Cry4*. The *ErCry4* data were reproduced four times using independently produced samples with comparable results. See Methods (Cavity ring-down spectroscopy) for further details.

Fig. 3 | EPR and optical spectroscopy of photo-induced FAD-Trp radical pairs in *ErCry4*.

a, Experimental conditions: 400 μM protein, pH 8.0, 20 mM Tris buffer, 20% glycerol.

The WT and W_dF spectra are averages of 100 measurements made, respectively, on three and two samples of each protein. Both spectra were reproduced once using independently produced samples with comparable results. See Methods (Electron paramagnetic resonance) for further details.

b, Experimental conditions: the samples contained 60% glycerol and were concentrated to 700 μM .

The WT and W_dF data are averages of 500 and 750 measurements, respectively, each on one sample. The WT and W_dF data were reproduced twice and three times, respectively, using independently

produced samples with comparable results. See Methods (Electron paramagnetic resonance) for further details.

c, Experimental conditions: 50-60 μM protein in 20 mM Tris buffer with ca. 200 mM NaCl, pH 8.0, with 20% glycerol and 1 mM $\text{K}_3\text{Fe}(\text{CN})_6$ at 5 $^\circ\text{C}$.

WT data are averages of 15 measurements on a single protein sample. Reproducibility was checked with two independently produced samples with comparable results. W₀F data are averages of measurements on a single protein sample. Reproducibility was checked with two independently produced samples with comparable results. See Methods (Picosecond transient absorption) for further details.

Fig. 4 | Reaction scheme and simulated magnetic field effects for *ErCry4*.

a, $\text{RP}_X = [\text{FAD}^{\bullet-} \text{Trp}_X\text{H}^{\bullet+}]$, the radical pairs formed by light-induced electron transfer along the chain of four Trp residues ($X = \text{A, B, C, D}$). $\text{RP}_{2X} = [\text{FAD}^{\bullet-} \text{Trp}_X^{\bullet}]$, the stabilised form of RP_X formed by deprotonation of $\text{Trp}_X\text{H}^{\bullet+}$ ($X = \text{C, D}$). Within the “composite radical pair” model, magnetic field effects on the quantum yield of the FADH^{\bullet} state arise from the rapidly interconverting RP_C and RP_D states via competition between back electron transfer (to give FAD^{ox}) and forward electron transfer (to form RP_{2C} and RP_{2D}). Reduction of Trp_X^{\bullet} (to Trp_XH) and protonation of $\text{FAD}^{\bullet-}$ (to FADH^{\bullet}) produces the potential signalling state which reverts slowly to the FAD^{ox} ground state.

b, Spin dynamics simulation for the reaction scheme shown at bottom left in which the curved arrows represent the coherent interconversion of the singlet (S) and triplet (T) states of a composite radical pair and the straight arrows indicate the competing reaction pathways. $\langle k_f \rangle$ and $\langle k_r \rangle$ are weighted averages of the corresponding rate constants for RP_C and RP_D . The contour plot shows the change in the yield of the $\langle k_f \rangle$ pathway caused by a 30 mT magnetic field as a function of $\langle k_f \rangle$ and $\langle k_r \rangle$. On the white line the lifetime of the composite radical pair is ≈ 100 ns. The positions of the white spots correspond to the rate constants estimated for RP_C and the composite pair with $f_C = 0.1$. See Methods (Spin dynamics calculations) and Supplementary Information (Rate constants of the reactions of the RPC/RPD composite radical pair) for further details.

c, As **b** except that the magnetic field is 50 μT and the white line corresponds to a lifetime of the composite radical pair of ≈ 1 μs . The white spots have been moved -1.0 log units along the $\langle k_f \rangle$ axis.

The custom code used to generate the contour plots in Fig. 4b and c (Wolfram Mathematica 12) is available at: http://hore.chem.ox.ac.uk/Nature_2021/Codes.zip.

Protein expression and purification

Full-length cDNA of *Erithacus rubecula* cryptochrome 4 (*ErCry4*, GenBank: KX890129.1) was cloned into the pCold expression vector as described previously³³ (TaKaRa, Shiga, Japan). The whole expression product consists of a translation enhancing element (the amino acid sequence is MNHKV), 10×His-tag, linker (sequence GGS), *SpeI* enzyme site (sequence TS) and *ErCry4*. Site-specific mutagenesis was performed with Q5® Site-Directed Mutagenesis Kit according the manufacturer's protocol (New England Lab, Ipswich, MA, USA). Forward and reverse primers were designed back to back with the desired nucleotide change in the centre of the forward primer using the online tool NEBaseChanger. Details of primer sequences are summarised in Table M1. Q5 Hot Start High-Fidelity DNA polymerase was used for the polymerase chain reaction. The cycle condition was 1 cycle of denaturation at 98 °C for 30 s; 25 cycles at 98 °C (10 s), 60 °C (17 s) and 72 °C (3 min), with a final extension of 10 min at 72 °C. Control sequencing was performed by an external contractor (LGC Genomics, Berlin, Germany). The expression construct of *Columba livia* (pigeon) cryptochrome 4 (*ClCry4*) was described previously³³. The full-length sequence of *Gallus gallus* (chicken) cryptochrome 4 (*GgCry4*) was cloned into the pCold vector with restriction enzyme sites of *SpeI* and *XbaI* following an identical protocol to that described above for *ErCry4*.

To express the protein, the expression construct was transferred into BL21(DE3) competent *E. coli* cells and then cultured on a lysogeny broth (LB) agar plate (tryptone 10 g/L, yeast extract 5 g/L, NaCl 10 g/L, agar 10 g/L, ampicillin 0.1 g/L) at 37 °C overnight. The monoclonal colonies were picked from the overnight-cultured LB agar plate and cultured in 30 mL LB medium (tryptone 10 g/L, yeast extract 5 g/L, NaCl 10 g/L, ampicillin 0.1 g/L) within a 150 mL Erlenmeyer flask as a starter cell culture. After incubation at 37 °C, 250 rpm for 6.0-6.5 h, the 30 mL cell culture starter was poured into 700 mL LB medium in each 2 L Erlenmeyer flask as the expansion culture. They were incubated at 37 °C, 200 rpm in shakers (Eppendorf, Hamburg, Germany). After 1.0-1.5 h, the cell density was measured in a 10 mm light-path cuvette (Ratiolab, Dreieich, Germany) at 600 nm using a Biophotometer plus (Eppendorf, Hamburg, Germany). As soon as the optical density at 600 nm (OD600) was 0.5-0.6, the shakers were set to 160 rpm, 15 °C. It took around 30 min to cool down to 15 °C. The temperature inside the shaker was read from the shaker screen and also double-checked (monitored) by two mercury thermometers, one placed at the rear wall of the shaker, the other in front of the shaker. The cell density was measured again when the cell culture reached 15 °C. OD600 readings were 0.9-1.1. Isopropyl-D-1-thiogalactopyranoside (IPTG) was added immediately into the cell culture. The optimal amount of IPTG varied among different proteins (5 µM IPTG for *ErCry4* WT, W369F, W372F, W318F; 2 µM IPTG for *ErCry4* W395F; 10 µM IPTG for *ClCry4* and *GgCry4*). Additionally, ampicillin was added at 71 µg/mL final concentration. The cells were incubated at 15 °C, 160 rpm for 20-22 h.

At this time, the cell culture was harvested by centrifugation at 4 °C, 7,000 rpm for 7 min in the 500 mL centrifuge bottles with a JLA-10.5 rotor (Beckman Coulter, Brea, CA, USA). The supernatant was discarded carefully and the cell pellet re-suspended with Ni-binding buffer (20 mM Tris, 150 mM NaCl, 5 mM imidazole, 10 mM 2-mercaptoethanol, pH 8.0). To re-suspend properly, the volume ratio of Ni-binding buffer and *E. coli* cell culture was 1:70. The cell suspension was transferred into 50 mL falcon tubes and re-centrifuged at 7,000 rpm for 7 min in a 5804R centrifuge (Eppendorf, Hamburg, Germany). The supernatant was discarded carefully and the cell pellet was stored at -20 °C for later processing.

To extract the protein, the cells were lysed by an ultrasonic homogeniser. First, the frozen cell pellet was thawed in a room-temperature water bath. Then the pellet was re-suspended with Ni-binding buffer. The volume ratio of Ni-binding buffer and *E. coli* cell culture was 1:70. Protease Inhibitor Cocktail Tablets (Roche) were added before lysis to inhibit general degradation of proteins (one tablet per 45 mL suspension). The 45 mL cell suspension was lysed using a 7 mm-diameter Sonotrode in a Hielscher UP200Ht ultrasonic homogeniser (Hielscher, Teltow, Germany) in an ice bath. The parameters were: power setting 170-200 W (the actual power delivered to the sample was 70 W), amplitude 100%. To prevent excessive heat generation, the lysis mode was 4 s Work / 8 s Break as one cycle. In total 120-

130 cycles were performed for each 45 mL cell suspension, with a 2 min break after the first 60-70 cycles. The following step was fractionation by centrifugation at 4 °C, 17,000 rpm for 40 min in the JA-25.5 centrifuge rotor (Beckman Coulter). The supernatant was separated carefully and was subjected to purification.

Purification was performed in two main steps: nickel affinity chromatography based on the His-tag and anion exchange chromatography based on the surface charge of the proteins. All the buffers were prepared with ultrapure water from arium® pro Water Systems (Sartorius, Göttingen, Germany), re-filtered by 0.22 µm Sartolab® RF Vacuum Filter (Sartorius) after preparation, and stored at 4 °C.

The Ni column contained 2.5 mL Ni-NTA matrix (Qiagen, Hilden, Germany), which was equilibrated with Ni-binding buffer. The lysed supernatant was loaded into equilibrated Ni-NTA columns. To avoid overloading, the volume ratio of supernatant and matrix was less than 20:1. Two or three columns were used if necessary. The supernatant flowed through the matrix by gravity at 4 °C, ca. 1 mL/min. Afterwards, the 2.5 mL Ni columns were washed with 200 mL Ni-wash buffer (20 mM Tris, 150 mM NaCl, 20 mM imidazole, 10 mM 2-mercaptoethanol, pH 8.0) by gravity-flow. The bound protein in the column was eluted competitively by introducing a high concentration of imidazole in Ni-elution buffer (20 mM Tris, 150 mM NaCl, 300 mM imidazole, 10 mM 2-mercaptoethanol, pH 8.0). The elution buffer was added onto the column 5 or 6 times, 2.5 mL at a time. The last drop out of the column opening was measured using a Bio-drop Spectrophotometer (Isogen Life Science, Utrecht, Netherlands) to determine the concentration. The elution was completed when the concentration was less than 0.05 mg/mL.

For further purification, anion exchange chromatography was performed with 5 mL Hitrap Q columns using an ÄKTA pure 25 M system (GE Healthcare, Sweden). It consisted of 6 steps: 1. sample preparation; 2. equipment equilibration; 3. sample manual loading; 4. sample application; 5. column wash; 6. gradient elution. To prepare samples for anion exchange chromatography, the eluted protein samples from the Ni columns were concentrated to 8-12 mg/mL (also measured by Bio-drop photometer). The samples were then diluted with 20 mM pH 8.0 Tris buffer by a factor of 2. The *ErCry4* and *GgCry4* samples were centrifuged at 13,000 rpm for 10-20 min and were then ready to load into the ÄKTA. The *ClCry4* samples needed to be re-concentrated to 8-12 mg/mL and diluted with 20 mM Tris (pH 8.0) by a factor of 2 again to reduce the salt concentration. Regarding the equipment preparation, pumps A and B of the ÄKTA were washed with 20 mL Buffer A (20 mM Tris, 75 mM NaCl for *ErCry4* and *GgCry4*, 37.5 mM NaCl for *ClCry4*, pH 8.0) and 20 mL Buffer B (20 mM Tris, 1 M NaCl, pH 8.0) respectively. The 5 mL sample loop and the whole path loop was washed with 10 mL Buffer A. The 5 mL Hitrap Q column was installed onto the ÄKTA under the condition of a low buffer flow rate (0.5 mL/min). Only when the top part of the column was filled with Buffer A, was the tubing connected to the top of the column to avoid any air bubbles. The column was then equilibrated with 40-50 mL Buffer A at a flow rate of 2 mL/min. To load the sample into the equipment, 4 mL supernatant was carefully drawn out from the centrifuged sample with a 5 mL syringe. Precipitate and air bubbles were avoided. The syringe was plugged onto the ÄKTA injection valve port and pushed slowly to load the sample into the 5 mL sample loop. Steps 4-6 were optimised and integrated as a processing program, which was stored in the UNICORN software (GE Healthcare, versions 7.1 and 7.3). For each purification, the following process was run: sample application 10 mL, 1 mL/min, 3 mL per fraction; column wash with 15 mL Buffer A, 2 mL/min, 3 mL per fraction; gradient elution from 0% to 50% Buffer B in 80 mL, 2 mL/min, 1.5 mL per fraction. *ErCry4* protein was eluted at a conductivity of ca. 20 mS/cm, *ClCry4* was eluted at a conductivity of ca. 10 mS/cm, and *GgCry4* was eluted at a conductivity of ca. 15 mS/cm. The fractions of the first peak during the gradient elution were identified as Cry4 by SDS-PAGE as well as in Western Blots. The fractions were then concentrated to 5-7 mg/mL, mixed with glycerol (20% volume ratio) and split into 100-200 µL aliquots in PCR tubes. The aliquots were shock-frozen with liquid nitrogen and stored at -80 °C for spectroscopic measurements. To maintain a reducing environment and avoid dimerization, 10 mM 2-mercaptoethanol (BME) was added to Buffer A and Buffer B at a late stage of the project. The protein samples were buffer-exchanged to remove BME in a Millipore centrifugation filter tube (Amicon Ultra, 30 kDa) prior each individual spectroscopic measurement.

Some of the spectroscopic measurements reported in the main text were obtained using *ErCry4* WT and *W_DF* samples containing one or two changes in the amino acid sequence at the extreme C-terminal end of protein. The data shown in [Fig. 2a and 2b](#) were recorded for sequences in which the last six amino acids (positions 522-527) were either AARTTD or AARTTE. A selection of the measurements were repeated with the correct sequence (VARTTE): the results were indistinguishable from those reported in the main text (Supplementary Information, [Fig. S3](#)).

Except where otherwise stated, protein concentrations in the spectroscopic measurements were determined using an extinction coefficient of 147,000 M⁻¹ cm⁻¹ at 280 nm.

Mutants	Primer sequences. F: Forward, R: Reverse
<i>ErCry4</i> W395F (<i>W_AF</i>)	F: 5'-TGCTGGGAAC TTT ATGTGGCTGT-3' R: 5'-TTGATACTGTAGTCAGCATCTAAAAG-3'
<i>ErCry4</i> W372F (<i>W_BF</i>)	F: 5'-GTGGATCAGC TTT GAAGAGGGGATGAAGGTG-3' R: 5'-AGGTCCCCCGTGTCTCAGG-3'
<i>ErCry4</i> W318F (<i>W_CF</i>)	F: 5'-CCAGATCTGC TTT TACAAGGATGCAGAGAGG-3' R: 5'-AGGCAGATGGGGTTCCCA-3'
<i>ErCry4</i> W369F (<i>W_DF</i>)	F: 5'-GGGGGACCTG TTT ATCAGCTGGG-3' R: 5'-CGTGTCTAGGAAGCAGGCG-3'

Table M1. Primers used for site-specific mutagenesis.

The mutagenesis sites are indicated in bold shaded font

Key resource table for protein expression and purification

Critical chemicals and reagents	Source	Identifier
Tryptone	OXOID	LP0042
Yeast extract	OXOID	LP0021
NaCl	Sigma	31434
Ampicillin sodium salt	Roche	K029.2
Isopropyl β -D-1-thiogalactopyranoside	Sigma	I5502-5G
Protease-inhibitor Cocktail Tablets	Roche	REF 04 693 132 001
Imidazole	Sigma	SZBE0500V
2-Mercaptoethanol	Sigma	M3148
Flavin adenine dinucleotide disodium salt hydrate	Sigma	089K1059
Coomassie Brilliant Blue R	Sigma	27816
Chromatography columns		
Econo-Pac® Chromatography Columns	BIO-RAD	7321010
Ni-NTA Agarose	QIAGEN	148053605
HiTrap Q HP	GE Healthcare	17-1154-01
Commercial Assays		
Site-Directed Mutagenesis Kit	NEB	E0552S
Rapid DNA Dephos & Ligation Kit	Sigma	4898117001
Critical Equipment		
New Brunswick Benchtop Shakers Innova 40R	Eppendorf	
Ultrasonic Homogeniser	Hielscher	HIEL_17002
High-speed centrifuge	Beckman Coulter	AVANTI J-E
ÄKTA Pure	GE Healthcare	
Filters		
Centrifugal Filters 30K	Amicon	UFC903096
Vacuum filter	Sartorius	180C5

Picosecond transient absorption (TA)

Transient absorption measurements were performed on a Ultrafast Systems EOS spectrometer modified for measurements of magnetic field effects on protein samples. Pump excitation was provided by a mode-locked picosecond Nd:YAG laser and OPG (Ekspla PL2210 and PG403), with a pulse width of 30 ps operating at a repetition rate of 1 kHz. The OPG was pumped with 200 μ J pulses at 355 nm, resulting in an energy at the excitation wavelength (450 nm) of approximately 30 μ J per pulse. The probe light source of the spectrometer is a supercontinuum white light laser with a range of 350-900 nm at a 2 kHz repetition rate. The spectrometer incorporates a set of home-built Helmholtz coils and a cryostat (Oxford Instruments OpistatCF) to accommodate the sample at the point of pump-probe overlap.

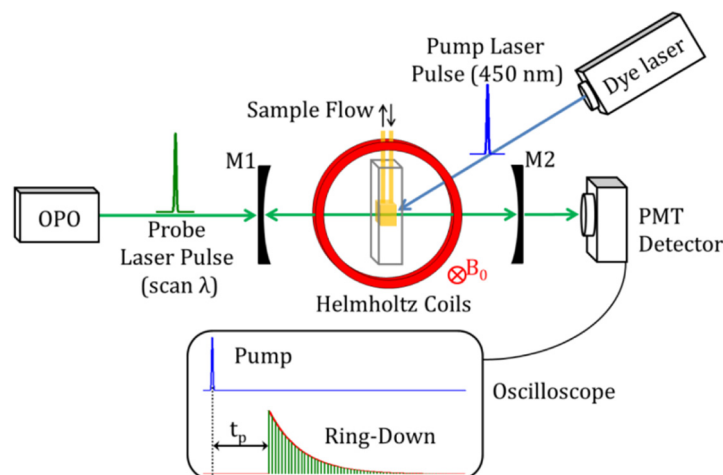
Samples were prepared by concentrating the expressed and purified proteins down to a volume of 200 μ L (150 μ L for W_DF) and an absorbance in the range 0.7-0.9 at 450 nm in a 1 cm path-length, 200 μ L quartz cuvette (Hellma) by centrifuging in a Millipore centrifugation filter (Amicon Ultra, 30 kDa). Buffer conditions for all measurements were 20 mM Tris buffer at pH 8.0, 200 mM NaCl, and 20% glycerol, unless otherwise stated. After concentrating the sample, 1 mM K₃Fe(CN)₆ was added and the sample was centrifuged at 5 °C for a minimum of 1 h to ensure the protein was in its fully oxidised state. Potassium ferricyanide was present in the sample during these measurements (and other experiments, as described below) to speed up the recovery of the photoreduced form of the protein and so reduce the time required to obtain spectra. As detailed in the Supplementary Information, addition of Fe³⁺ was found by CRDS to have no effect on the magnetic sensitivity of ErCry4 W_DF.

Measurements were made with the cuvette placed in the cryostat at a temperature of 5 °C. Magnetic field effect experiments consisted of a total of 10-15 experimental repeats. Each repetition consisted of one measurement of the transient absorption signal made with the field ON (25 mT) and one with the field OFF (0 mT). The starting field conditions were alternated (from ON to OFF, or OFF to ON) between experimental repeats. In each ON or OFF step, the signal was collected for a total photolysis time of 3 min before the field condition was changed. To minimise photodamage and to allow for reoxidation of the sample, data were collected in increments of 15 s, followed by a 3 min wait time (5 min for W_DF and WT) before the next increment.

Labview code was written to average experimental repetitions, and to average over time or wavelength regions of the dataset as necessary. Magnetic field effects were calculated as a difference between the transient absorption signal from the field ON and field OFF measurements: $\Delta\Delta A = \Delta A(25 \text{ mT}) - \Delta A(0 \text{ mT})$.

Cavity ring-down spectroscopy (CRDS)

CRDS measurements were made on a home-built spectrometer (schematic below) based on that described by Maeda *et al.*³⁴ A quartz flow cell (Hellma, 165-QS, 0.2 mL sample volume, 1 mm path length) was situated in the centre of a 0.6 m optical cavity comprised of two highly reflective mirrors M1 and M2 (Layertec, broadband coated, radius of mirror curvature 0.5 m, reflectivity > 99.7% in the wavelength range 450-690 nm). A Nd:YAG (Continuum, Surelite I) pumped dye laser (Sirah, Cobra) was used for photoexcitation at 450 nm. Measurements were performed with 0.3 mJ light pulses at 1 Hz. Probe light was generated by a tunable optical parametric oscillator (Opotek, Opolette) and introduced into the cavity via the front mirror M1. Light leaving the rear mirror M2 was detected by a photomultiplier tube (Hamamatsu, H6780) and recorded on a digital oscilloscope (LeCroy, WaveSurfer 64MXs-A). An external magnetic field (0-30 mT) was applied using a set of home-built Helmholtz coils. Protein samples were maintained at 278 K during measurements using a temperature-controlled circulating bath (Grant, Optima T100). Experiments on cryptochromes were performed without flowing the samples.



Schematic of the CRDS apparatus used to measure radical concentrations as a function of time after the pump pulse and magnetic field strength.

The light intensity exiting the cavity via M2 was measured alternately with and without photoexcitation. The change in the per-pass absorbance, ΔA , was calculated from the ring-down times recorded with, τ , and without, τ_0 , photoexcitation, using

$$\Delta A = \frac{1}{\ln(10)} \frac{L}{c} \frac{\tau_0 - \tau}{\tau_0 \tau}$$

where L is the length of the cavity and c the speed of light³⁴.

ΔA signals were recorded at specific time intervals after photoexcitation by varying the pump-probe delay time which was controlled by digital delay generators (Quantum Composer, 9520; Stanford Research Systems, DG645). Differential absorbance spectra were recorded by scanning the probe wavelength (λ) in steps of 10 nm. Further details can be found in Maeda et al.³⁴

Unless otherwise stated, measurements were made on 200 μL samples of 60–70 μM protein in 10 mM Tris solution at $\text{pH} \approx 7$ with 250 mM NaCl, 5 mM $\text{K}_3\text{Fe}(\text{CN})_6$ and 20% v/v glycerol at 278 K.

Broadband cavity-enhanced absorption spectroscopy (BBCEAS)

BBCEAS measurements were made on a home-built spectrometer based on that described by Neil et al.³⁵. The following summarises the changes made to the instrumentation and experimental methodology.

The optical cavity consisted of two high-reflectivity mirrors (> 0.9993 , Layertec R400–800 nm) and a temperature controlled quartz sample cell (1 mm path length, 180 μL capacity, Hellma Analytics, 165-QS). The cavity was injected with light from a broadband supercontinuum laser (ca. 580 mW, 390–780 nm, SuperK Extreme EXU-6, NKT Photonics) and the cavity output was dispersed using a spectrograph (600 lines/nm, Andor Shamrock) and measured with a CCD camera (Andor Newton). The 3 mW 450 nm pump beam (Oxxius, LBX-450) was guided to the sample by two turning mirrors. Both of the lasers were equipped with fast (< 2 ms switch time) shutters. The magnetic field was provided by a purpose-made set of water-cooled magnetic field coils. The magnetic field could be varied in the range +30 to -30 mT with a 80 ms rise time. A custom three-dimensional Hall probe was used to continuously adjust the field

over the course of the experiment, and its readings were regularly calibrated against a commercial gaussmeter (ca. $\pm 10 \mu\text{T}$ accuracy, Lakeshore 425).

During the experiment the sample was measured for ca. 10 s and then allowed to re-oxidise in the dark for 20 min. Each measurement was a 10 s long continuous camera acquisition. Over the first 200 ms, only the supercontinuum light was present in order to measure the sample in the ground state. This was followed by the pump beam shutter being open for ca. 9 s to observe the light-induced change in the sample absorbance. While this was happening, the magnetic field was switched on to a constant value and off with a period of 400 ms. Light-induced change in samples absorbance (ΔA) could therefore be ascertained. The field-switching times were well calibrated such that the field at any time point was known and the data could be easily divided into 'field-on' and 'field-off' measurements. The last 50 ms of each step were used for analysis. A line was fitted to each pair of neighbouring off-steps and compared to the intermediate on-step. Special care was taken not to introduce magnetic field effect artifacts over the course of this analysis. The corresponding magnetic field effect ($\Delta\Delta A$) was obtained by analysing the magnitude of steps in ΔA . In order to obtain the data shown in Fig. 2a, b, ($\Delta\Delta A$ as a function of the strength of the magnetic field), the above procedure was repeated for a range of magnetic field strengths during the on-steps.

Before use the sample cells were cleaned with concentrated HNO_3 . They were then neutralised and further cleaned with a commercial optics cleaning solution (Hellmanex), a 40:60 mixture of acetone:methanol to achieve high optical quality. The calibration procedure (broadly as described previously³⁵) was then performed, and the cell was pre-washed with 20% v/v glycerol and buffer to minimise the effects of mixing with any water leftover from the calibration. The protein samples were prepared in 20% v/v glycerol, 50 mM HEPES buffer with 100 mM NaCl, and kept in the dark until transferred into the measurement cell. They were then allowed to rest in the dark for at least 30 min to settle before any measurements.

The magnetic field setting was done with a programmable waveform generator (Rigol, DG1022Z). The timing of the experiment was controlled with a digital delay generator (Stanford Research Systems, DG645). The control of all of the parts of the instrument — setting up the timing and field settings as well as the data collection after each acquisition, was done with a LabVIEW (2015) program. The data analysis was done in Matlab.

The cavity output was coupled into the spectrograph by means of a periscope. The light was coupled into the spectrograph with a matched-pair broadband achromat. The spectra were collected at ca. 0.6 nm wavelength resolution (1024 points between 300 and 900 nm) with 3 ms per frame continuous exposure. Only the bottom 30 pixels of each frame were collected (crop mode) to improve time resolution, and were then binned into a one-dimensional, wavelength-resolved spectrum. The camera had a 16-bit well depth, and dark noise of 310 counts. This allowed spectra to be collected with a relatively large dynamic range

The optical cavity was 20 cm long with the sample cell positioned in the middle. The sample cell was secured in a 3D-printed plastic mount (PLA, solid infill), in a gimbal mount (Thorlabs, GM200/M). For all of the protein samples the temperature of the cell was kept at 5 °C by means of a recirculating chiller. The temperature was calibrated to account for any losses between the chiller and the cell. The space between the mirrors and the sample cell was protected from dust with SM1 tubes and was kept under a slight positive pressure of dry air. This was done to prevent dust entering the cavity and to avoid condensation on the sample cell. Furthermore, the entire optical cavity, including the magnetic field coils was kept in a custom-made enclosure filled with dry air. This was to further protect the sample cell from condensation as well as to limit the effect of air currents on the stability of the cavity.

Continuous photoreduction

ErCry4 protein samples were fully oxidised using 1 mM $\text{K}_3\text{Fe}(\text{CN})_6$. The oxidizing agent was then removed by placing 200 μL samples in a 30 kDa Amicon centrifuge filter tube in a temperature-cooled microcentrifuge and washing with 20 mM Tris buffer, 260 mM NaCl, pH 8.0, 20% glycerol containing 5 mM dithiothreitol. Protein samples were placed in a Hellma microvolume cuvette inside a Peltier-cooled sample holder (278 K) within a Carey 60 UV-vis spectrophotometer and irradiated using a 3.5 mW 450 nm LED and a diffuser to ensure uniform excitation. Spectra (200-800 nm) were recorded at intervals after the start of continuous irradiation.

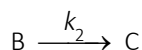
Re-oxidation experiments

Samples of protein were prepared in a pH 8.0 Tris buffer (20 mM) containing 200 mM NaCl and 20% glycerol. The β -mercaptoethanol (BME) that had been added during purification (to prevent oligomerisation) was removed by concentrating samples to 200 μL in a 30 kDa Amicon centrifuge followed by washing with an equivalent, but BME-free, buffer. Where necessary, 1.5-2.5 mM $\text{K}_3\text{Fe}(\text{CN})_6$ was then added to oxidise the small fraction of protein present in the FADH^\bullet state, followed by a further wash with BME-free buffer to remove Fe(II) and Fe(III). The final sample volume was typically around 150 μL with a concentration of ca. 35 μM (0.4 absorbance at 450 nm).

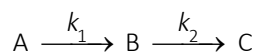
Experiments were performed in an Agilent Cary 60 UV-vis spectrophotometer, using a custom sample mount including a 450 nm LED (Luxeon, Rebel, Royal Blue, SR-12-RA900, $\lambda_{\text{max}} = 447.5 \text{ nm}$, $\lambda_{50\%} \approx 440, 460 \text{ nm}$). The sample was placed in a quartz cuvette with windows on three sides (Hellma, ultra-micro cell, 105-250-85-40), with the largest window (10 mm \times 5 mm) facing the LED. The two smaller windows (2 mm \times 5 mm), on opposite sides of the cuvette, were used for the UV-vis light. Samples were irradiated for 2 min at 20 $^\circ\text{C}$. Spectra were then recorded at 6, 15 or 30 s intervals, typically for a total of 90 min. Experiments were performed under aerobic conditions (the open cuvette was in contact with room air) with no added oxidants or reductants.

A Gentec XLP12-3S-H2-D0 thermopile detector was used to measure the intensity of the LED light at the sample. Two irradiances were used: 260 $\mu\text{mol m}^{-2} \text{s}^{-1}$ ("low power") and 2,600 $\mu\text{mol m}^{-2} \text{s}^{-1}$ ("high power"). Typically, the irradiated samples had reached a steady state after 2 min irradiation, with a loss of ca. 50% of the absorbance at 450 nm.

A global analysis procedure was used with kinetic models



for the lower power experiments and



for the high power experiments. k_1 and k_2 are first order rate constants. Fitting to a complete sets of time-dependent spectra gave estimates of k_1 and k_2 , the fractional initial concentrations of the two or three species and the species-associated spectra (SAS). Species A, B and C were assigned to FADH^- , FADH^\bullet and FAD^{ox} (Supplementary Information).

Electron paramagnetic resonance (EPR)

Transient continuous wave EPR measurements

Time-resolved continuous wave (cw) EPR measurements were carried out on a Bruker ELEXSYS E680 spectrometer operated at X-band frequencies (9.75 GHz) using a Bruker MD5 resonator (ER4118X-MD5). The temperature was held constant at 274 K using a nitrogen gas-flow cryostat.

Protein solutions with a concentration of 400 μM (20% glycerol, 5 mM $\text{K}_3\text{Fe}(\text{CN})_6$) were prepared and transferred to a quartz tube with inner and outer diameters of 0.7 mm and 0.9 mm, respectively. For the measurement, the tube containing the sample was inserted into larger quartz tubes to mount the sample in a straight and reproducible orientation and optimise the filling factor of the cavity. A cavity quality factor of 1800 could be obtained this way.

The samples were photo-excited at 450 nm with 2 mW pulses of 5 ns duration using an OPO pumped by the third harmonic of a Nd:YAG laser (Opotek, Opolette) operated at a repetition rate of 1 Hz. Before reaching the sample, the excitation light was depolarised.

The time-resolved cw EPR spectra were acquired in direct detection mode using a transient recorder and a microwave power of 2 mW (20 dB). For every field value, a time trace with 2048 points was recorded using a time base of 2 ns. Considering a background of about 600 ns before the laser pulse, these settings resulted in a time window of about 3.5 μs . After data acquisition, the two-dimensional spectra were baseline-corrected in both dimensions using a home-written Matlab routine. The spectra shown in Fig. 3a were averaged over a time window from 0.1 μs to 0.9 μs after laser excitation and the spectral shape was found not to change significantly with time.

The spectra were field-corrected using a BDPA field standard ($g = 2.00242$) and frequency-corrected to 9.75 GHz.

The signals of several identical samples were averaged to obtain the spectra shown in Fig. 3a. Every sample was measured for about 2-3 h during which several spectra were recorded (with different sweep directions, i.e. field up-down and down-up, to compensate for sample degradation) and averaged.

Out-of-phase electron spin echo envelope modulation (OOP-ESEEM) measurements

OOP-ESEEM measurements were carried out on a Bruker ELEXSYS E580 spectrometer operated at Q-band frequencies (34 GHz) using a Bruker D2 resonator (EN5107D2). The temperature was held constant at 80 K using a nitrogen gas-flow cryostat.

Protein solutions with a concentration of 700 μM (60% glycerol, 5 mM $\text{K}_3\text{Fe}(\text{CN})_6$, 20 mM Tris buffer, pH 8, 260 mM NaCl) were prepared and transferred to a quartz tube with inner and outer diameters of 1 mm and 1.6 mm, respectively. The samples were frozen in liquid nitrogen before being inserted into the EPR resonator cooled to 80 K.

The samples were photo-excited at 450 nm with 1 mJ laser pulses of 5 ns duration using an OPO pumped by the third harmonic of a Nd:YAG laser (Opotek, Opolette) operated at a repetition rate of 20 Hz. Before reaching the sample, the excitation light was depolarised.

After sample illumination, the rapid build-up of a strong background signal from a stable flavin-based (dark state) radical was observed. The pulse sequences therefore needed to be adapted in order to minimise the contribution of this background signal to the detected, light-induced, signal. The dark state radical signal was used to correctly phase the transient signals.

When recording echo-detected field-swept EPR spectra, an emissive signal was observed in the imaginary channel (out-of-phase signal) with its maximum intensity at the field position corresponding to the zero-crossing point of the (emissive/absorptive) radical pair signature recorded in the real channel.

The OOP-ESEEM experiments were carried out at a magnetic field position corresponding to the intensity maximum of this out-of-phase signal using the microwave pulse sequence $(\xi_1)_{\text{xx}}-T-h\nu-t_{\text{DAF}}-(\xi_2/2)_x-\tau-(\xi_2)_x-\tau$ -echo with $T = 10 \mu\text{s}$ and delay-after-flash, $t_{\text{DAF}} < 100 \text{ ns}$. The pulse flip angle ξ_1 was optimised by adjusting the power of a 16 ns pulse until the dark state echo signal was reduced to a minimum. The flip angle ξ_2 (corresponding approximately to π) was optimised to maximise the OOP echo intensity. The microwave pulses of the echo detection sequence had lengths of 8 and 16 ns, respectively. In the experiment, the inter-pulse delay τ was varied from 80 ns to 2 μs in steps of 4 ns

and the OOP echo intensity was recorded as a function of τ to obtain the data shown in Fig. 3b.

Key resource table for spectroscopic experiments

Critical chemicals and reagents	Source	Identifier
Tris buffer	Sigma Aldrich	10708976001
HEPES buffer	Sigma Aldrich	H3375-25G
NaCl	Sigma Aldrich	S7653-250G
K ₃ Fe(CN) ₆	Sigma Aldrich	702587-250G
Dithiothreitol	Sigma Aldrich	10197777001
Glycerol	Sigma Aldrich	G9012-500ML
Equipment for transient absorption		
TA spectrometer	Ultrafast Systems	EOS
Nd:YAG laser	Ekspla	PL2210
OPG laser	Ekspla	PG403
Cryostat	Oxford Instruments	OpistatCF
Equipment for CRDS		
Nd:YAG laser	Continuum	Surelite I
Dye laser	Sirah	Cobra
Optical parametric oscillator	Opotek	Opolette
Photomultiplier tube	Hamamatsu	H6780
Digital oscilloscope	LeCroy	WaveSurfer 64MXs-A
Digital delay generator	Quantum Composer	9520
Digital delay generator	Stanford Research Systems	DG645
Equipment for BBCEAS		
Supercontinuum laser	NKT Photonics	SuperK Extreme EXU-6
Spectrograph	Andor	Shamrock
CCD camera	Andor	Newton
Pump laser	Oxxius	LBX-450
Gaussmeter	Lakeshore	425
Waveform generator	Rigol	DG1022Z
Digital delay generator	Stanford Research Systems	DG645
Equipment for photoreduction and re-oxidation expts		
UV-vis spectrophotometer	Carey	60
LEDs	Luxeon	SR-12-RA900
Micro cell	Hellma	105-250-85-40
Equipment for EPR		

X-band EPR spectrometer	Bruker	ELEXSYS E680
X-band resonator	Bruker	ER4118X-MD5
Nd:YAG laser	Opotek	Opolette
Q-band EPR spectrometer	Bruker	ELEXSYS E580
Q-band resonator	Bruker	EN5107D2

Spin dynamics calculations

Magnetic field effects on the product yields of $[\text{FAD}^{\bullet-} \text{TrpH}^{\bullet+}]$ radical pairs (Fig. 4b and 4c) were calculated for the reaction scheme shown in Fig. 4a. The spin Hamiltonians of the two radicals were

$$\hat{H} = \hat{H}_1 + \hat{H}_2, \quad (\text{M1})$$

$$\hat{H}_i = \gamma_e B \hat{S}_{iz} + \gamma_e \sum_j a_{ij} \hat{S}_i \cdot \hat{I}_j, \quad (\text{M2})$$

where \hat{S}_i is the electron spin operator for radical i , \hat{I}_j is the spin operator of nucleus j , and a_{ij} is the hyperfine coupling constant of nucleus j in radical i . The magnetic field strength was $B = 30$ mT (Fig. 4b) or 50 μT (Fig. 4c). We assumed the anisotropic components of the hyperfine interactions and the electron spin couplings were averaged to zero by molecular tumbling. The following isotropic hyperfine interactions were included: in $\text{FAD}^{\bullet-}$ N5 ($a = 14.65$ MHz) and N10 ($a = 5.28$ MHz); in $\text{TrpH}^{\bullet+}$ N1 ($a = 9.00$ MHz)⁴⁶. The exchange interaction was assumed to be zero.

The master equation for the radical pair density matrix, $\hat{\rho}(t)$, is

$$\frac{d\hat{\rho}(t)}{dt} = -\hat{L}\hat{\rho}(t) \Rightarrow \hat{\rho}(t) = e^{-\hat{L}t} \hat{\rho}(0) \quad (\text{M3})$$

where the Liouvillian, \hat{L} , is

$$\hat{L} = i\hat{H} + \frac{1}{2}\langle k_r \rangle \hat{Q}_s + \langle k_f \rangle \hat{E} + \hat{W}. \quad (\text{M4})$$

\hat{H} is the Hamiltonian commutator superoperator, \hat{Q}_s is the singlet projection superoperator, and \hat{E} is the identity superoperator:

$$\hat{H}\hat{\rho}(t) = \hat{H}\hat{\rho}(t) - \hat{\rho}(t)\hat{H}, \quad (\text{M5})$$

$$\hat{Q}_s\hat{\rho}(t) = \hat{Q}_s\hat{\rho}(t) + \hat{\rho}(t)\hat{Q}_s. \quad (\text{M6})$$

We assume a random fields electron spin relaxation mechanism for both radicals with relaxation rate constant, $k_{\text{RFR}} = 10^6 \text{ s}^{-1}$:

$$\hat{W}\hat{\rho}(t) = k_{\text{RFR}} \sum_i \sum_{p=x,y,z} \left[\hat{S}_{ip}, [\hat{S}_{ip}, \hat{\rho}(t)] \right]. \quad (\text{M7})$$

The fractional yield of the k_f pathway once all radical pairs have reacted was calculated as

$$\Phi_f = \langle k_f \rangle \int_0^\infty \text{Tr}[\hat{\rho}(t)] dt = \langle k_f \rangle \text{Tr} \left[\hat{L}^{-1} \hat{\rho}(0) \right]. \quad (\text{M8})$$

The initial state of the radical pair was a pure singlet. The quantity plotted in Fig. 4b and 4c is $\Phi_f(B) - \Phi_f(0)$.

Molecular dynamics simulations of *ErCry4*

A three-dimensional structure of *ErCry4* was built using the Swiss-model workspace⁴⁷ with the amino acid sequence in Ref.²⁵ and pigeon Cry4 (PDB ID: 6PU0)¹⁵ as a template for the homology model. This homology model comprised residues 8-495 of the *ErCry4* sequence. No structural data were available as a template for residues 1-7 or 496-527; they were consequently excluded from the model.

The homology model of the ground state of *ErCry4* was solvated, neutralised and then energy-minimised for 10,000 conjugate-gradient steps. It was dynamically equilibrated for 5 ns, using the NAMD 2.10 molecular dynamics (MD) package⁴⁸, followed by a 200 ns production simulation. Five more MD simulations were performed corresponding to four radical pair states of *ErCry4*: [FAD^{•−} Trp_AH^{•+}] (RP_A), [FAD^{•−} Trp_BH^{•+}] (RP_B), [FAD^{•−} Trp_CH^{•+}] (RP_C) and [FAD^{•−} Trp_DH^{•+}] (RP_D), and the ground state of the W_DF mutant. The simulation protocol is summarised in Table M2. The four-stage equilibration protocol was used as described in Ref. ^{49,50 51} and was implemented in the VIKING platform for multiscale simulations⁴⁹. Stage 0 was the energy minimisation; in Stage 1 water molecules and ions were equilibrated, keeping the protein harmonically constrained; in Stage 2 the atoms of the sidechains were released and equilibrated; and finally the entire system was equilibrated in Stage 3 prior to the production simulation.

All simulations were carried out using the CHARMM36 force field⁵²⁻⁵⁴ for proteins with CMAP corrections, together with parameterisations for FAD^{55,56}, FAD^{•−} ⁵⁶, and TrpH^{•+} ⁵⁵, that have been successfully employed in several previous MD studies of cryptochromes from other species^{50,55-58}. In all simulations, Na⁺ ions were added to neutralise the system, and then additional Na⁺ and Cl[−] ions were added to achieve a NaCl concentration of 50 mM.

An integration time-step of 2 fs was used for production simulations and the temperature was controlled at 310 K using the Langevin thermostat with a damping coefficient of 5.0 ps^{−1}, applied to all atoms in the system, except hydrogens. Similarly, the pressure was held at 1 atm with the Langevin Barostat⁵⁹ in equilibration simulations. The ShakeH algorithm (a standard component of NAMD) was used to keep bonds involving hydrogen atoms at fixed lengths. Periodic boundary conditions were adopted in all MD simulations and the Particle Mesh Ewald summation method⁶⁰ was employed for evaluating Coulomb forces. The van der Waals energy was calculated using a smooth cut-off distance of 12 Å with a switching distance of 10 Å. Analysis of the obtained MD results was performed using VMD 1.9.3⁶¹ and VIKING 1.0⁴⁹.

<i>ErCry4</i> state	Equilibration phase				Production simulation	System information	
	<i>Stage 0</i> Minimisation	<i>Stage 1</i> Water and ions	<i>Stage 2</i> Water, ions and side chains	<i>Stage 3</i> All atoms		Box size/ Å	Number of atoms
GS	100,00 steps	<i>NPT</i> , 1 ns	<i>NPT</i> , 2 ns	<i>NVT</i> , 2 ns	<i>NVT</i> , 200 ns	92.08 × 104.86 × 100.31	100,518
RP _A RP _B RP _C RP _D	—	—	—	<i>NVT</i> , 2 ns	<i>NVT</i> , 200 ns	92.08 × 104.86 × 100.31	100,518
W _D F	—	—	—	<i>NVT</i> , 2 ns	<i>NVT</i> , 200 ns	92.08 × 104.86 × 100.31	100,514

Table M2. Summary of the MD simulation protocol. The table lists the six simulations carried out. GS = ground state (FAD^{ox} and all four Trp residues in their ground states). See text for the other abbreviations. The GS simulation included all four stages of equilibration. The other five states were constructed using the final snapshot of the GS simulation, and therefore only required Stage 3 equilibration.

Quantum chemical calculations of FAD, FAD^{•−}, TrpH, and TrpH^{•+} self-energies

Representative self-energies of FAD, FAD^{•−}, TrpH, and TrpH^{•+} were established to permit estimates of the different intra-*ErCry4* electron transfer rate constants. These calculations were done for 20 configurations of *ErCry4*, selected randomly from the production MD simulation of the GS state (Table M2). For the 20 configurations, the structures of the entire FAD cofactor and the Trp_D residue were selected using the VIKING platform⁴⁹. Hydrogen atoms were added to terminate dangling polypeptide bonds in the Trp_D structures.

Single-point energies were computed for the selected 20 geometries of the FAD cofactor in its FAD and FAD^{•−} states, and for the terminated Trp residue in its TrpH and TrpH^{•+} states. The density functional theory CAM-B3LYP method⁶² was used in all calculations, while the standard 6-31G basis set was employed to expand the electronic wavefunctions, as implemented in the Gaussian 09 program⁶³. The energies of FAD, FAD^{•−}, TrpH and TrpH^{•+} were calculated by setting the total charge and multiplicity to correspond to the closed-shell or radical form. The configurations were extracted from MD simulations and were not geometry-optimised. Geometry optimisation in vacuum would not have been representative of the cofactors' configurations in the *ErCry4* structure, while optimisation taking accurate account of the environment would have been computationally demanding. We have therefore chosen a sufficient number of molecular configurations directly from the MD simulations, and ensured

that the resulting energies of FAD, FAD^{•−}, TrpH and TrpH^{•+} follow gaussian distributions. There were only minor differences (1-2 kcal mol^{−1}) between the single-point energies of FAD^{•−} and TrpH^{•+} taken from the GS simulation and from the RP_A–RP_D simulations, as the radicals have very similar internal conformations in all simulations. Therefore, only the snapshots taken from the GS simulation were used.

Average values, representing the self-energies for the redox cofactors FAD, FAD^{•−}, TrpH, and TrpH^{•+}, were obtained from the single-point energies for the 20 snapshots.

Electron transfer rate constants

To compute the electron transfer rate constants, one has first to establish the total energy of the system in different redox states. Molecular mechanics force fields provide a poor estimate for the self-energy of FAD, FAD^{•−}, TrpH, and TrpH^{•+} in *ErCry4*, because they are essentially parameterised to describe the interactions of these species with the other components of the simulation. To obtain an improved self-energy it is possible to calculate the total energy of the system by combining data obtained from MD simulations with the self-energies that follow from quantum chemical (QC) calculations. The total energy of the system in a particular redox state can thus be calculated as:

$$E_{a|s} = E_{a|s}^{(MD)} - \left(E_{FAD}^{(MD)} + E_{Trp}^{(MD)} \right)_{a|s} + \left(\left\langle E_{FAD}^{(QC)} \right\rangle + \left\langle E_{Trp}^{(QC)} \right\rangle \right)_{a|s}. \quad (M9)$$

The subscript *a* denotes the electronic configuration of the active site comprised of FAD, Trp_A, Trp_B, Trp_C, and Trp_D, each of which is either in its closed-shell or radical form. The subscript *s* denotes the equilibrium state of the rest of the protein (i.e. GS, RP_A, RP_B, RP_C, or RP_D). For example, $E_{RP_A|DS}$ is the total energy of the system immediately after the formation of the radical pair FAD^{•−} Trp_AH^{•+} from the ground state before the remainder of the protein has had time to relax. The first term in Eqn (M9) corresponds to the total energy of the system, as obtained from MD simulations. The second term represents the MD self-energy of the electron transfer donor and acceptor molecules, while the last term is the average QC energy of these molecules. The results of the QC calculations for 20 independent snapshots are compiled in [Table S4](#) together with the mean values.

Here we have studied the electron transfers RP_A ↔ RP_B, RP_B ↔ RP_C, RP_C ↔ RP_D, RP_C → GS, and RP_D → GS. The free energy change associated with these electron transfer reactions and the corresponding rate constants can be obtained from the difference between the reactant and the product energy minima⁶⁴⁻⁶⁶. Following the definition in Eqn (M9), the corresponding energy gaps can be defined as:

$$\Delta E_{\text{react}} = E_{\text{react|prod}} - E_{\text{react|react}}, \quad (M10)$$

$$\Delta E_{\text{prod}} = E_{\text{prod|prod}} - E_{\text{react|prod}}. \quad (M11)$$

The energy gaps for the RP_A ↔ RP_B, RP_B ↔ RP_C, RP_C ↔ RP_D electron transfer reactions are shown in [Fig. S9](#), and for the RP_C → GS, RP_D → GS reactions in [Fig. S10](#). These energy gaps follow a Gaussian-like distribution that defines a probability density distribution:

$$p(\Delta E_i) = \sqrt{\frac{2}{\pi \sigma_i^2}} \exp \left(-\frac{2[\Delta E_i - \langle \Delta E_i \rangle]^2}{\sigma_i^2} \right). \quad (M12)$$

The subscript *i* corresponds to the reactant or product states, σ_i is the width of the distribution, and $\langle \Delta E_i \rangle$ is the average energy gap for a particular probability distribution $p(\Delta E_i)$. The free energy could be readily calculated once $p(\Delta E_{\text{react}})$ and $p(\Delta E_{\text{prod}})$ are known⁶⁵⁻⁶⁷:

$$G_i(\Delta E_i) = -k_B T \ln[p(\Delta E_i)] + G_i^{(0)} \quad (\text{M13})$$

Fig. S9 and S10 show the resulting free energy curves. The definition of the free energy in Eqn (M13) implies that the energy profiles for the reactant and product states cross at $\Delta E=0$, which is achieved by shifting the energy of one state relative to the other by choosing appropriate $G_i^{(0)}$ values^{65,66}.

The free energy profiles in Fig. S9 and S10 allow one to determine the reorganisation energies λ and driving forces ΔG for all electron transfer processes of interest. The obtained values are summarised in Table S3 and can be used to estimate the electron transfer rate constants using the following expression⁶⁸⁻⁷¹:

$$\log_{10} k = 13 - 0.6(R-3.6) - 3.1 \frac{(\Delta G + \lambda)^2}{\lambda} \quad (\text{M14})$$

Where R is in Å and ΔG and λ are in eV. The obtained values of the electron transfer rate constants are given in Table S3.

Code availability

The custom codes used to generate the contour plots in Fig. 4b and c (Wolfram Mathematica 12) and the simulations in Fig. S4 (Wolfram Mathematica 12) can be downloaded from: http://hore.chem.ox.ac.uk/Nature_2021/Codes.zip.

The custom codes written to control and acquire data from our home-built magnetic field effect spectrometers (LabView v.15 and C++) are available from PJH on request.

NAMD 2.10 (<http://www.ks.uiuc.edu/Research/namd/>)⁴⁸ was used for the molecular dynamics simulations.

VMD 1.9.3 (<http://www.ks.uiuc.edu/Research/vmd/>)⁶¹ was used for analysis of molecular dynamics data.

NAMD and VMD are open source codes.

All relevant input (430 MB) and output files for the molecular dynamics simulations and quantum chemistry calculations can be downloaded from the University of Oldenburg repository: <https://cloud.uol.de/s/NrTYpoEzL6RbPq7>.

Additional information

Supplementary Information is available for this paper.

Correspondence and requests for materials should be addressed to:

peter.hore@chem.ox.ac.uk, henrik.mouritsen@uni-oldenburg.de,
stuart.mackenzie@chem.ox.ac.uk, christiane.timmel@chem.ox.ac.uk, canxie@hmfl.ac.cn,
ilia.solovyov@uni-oldenburg.de.

Reprints and permissions information is available at www.nature.com/reprints.

Supplementary Information

UV-visible spectra of *ErCry4* WT and W_xF mutants

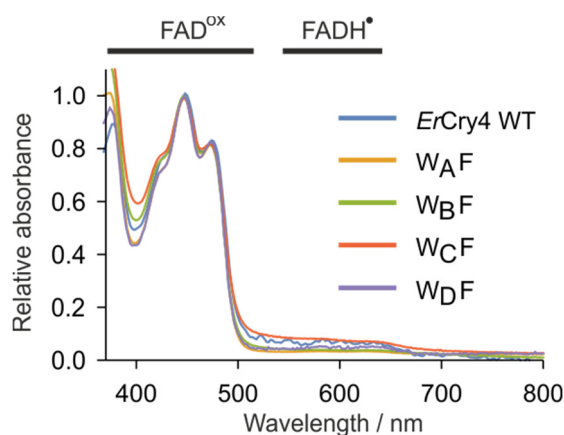


Fig. S1. UV-visible spectra of *ErCry4* WT and W_xF mutants.

For all five proteins, the FAD absorption band centred at 450 nm shows the vibronic fine structure at ~480 nm characteristic of a cryptochrome-bound flavin¹². The weak absorbance signals at 500-650 nm arise from small amounts of reduced protein containing $FADH^\bullet$. Virtually identical UV-visible spectra exist for all protein samples measured. Regarding the total number of each type of samples, please see statistics and reproducibility information related to Fig. 1a and 1b. For the total number of each type of sample, see Statistics and Reproducibility information for Fig. 1a and 1b.

Transient absorption kinetics and spectra of *ErCry4* WT and mutants

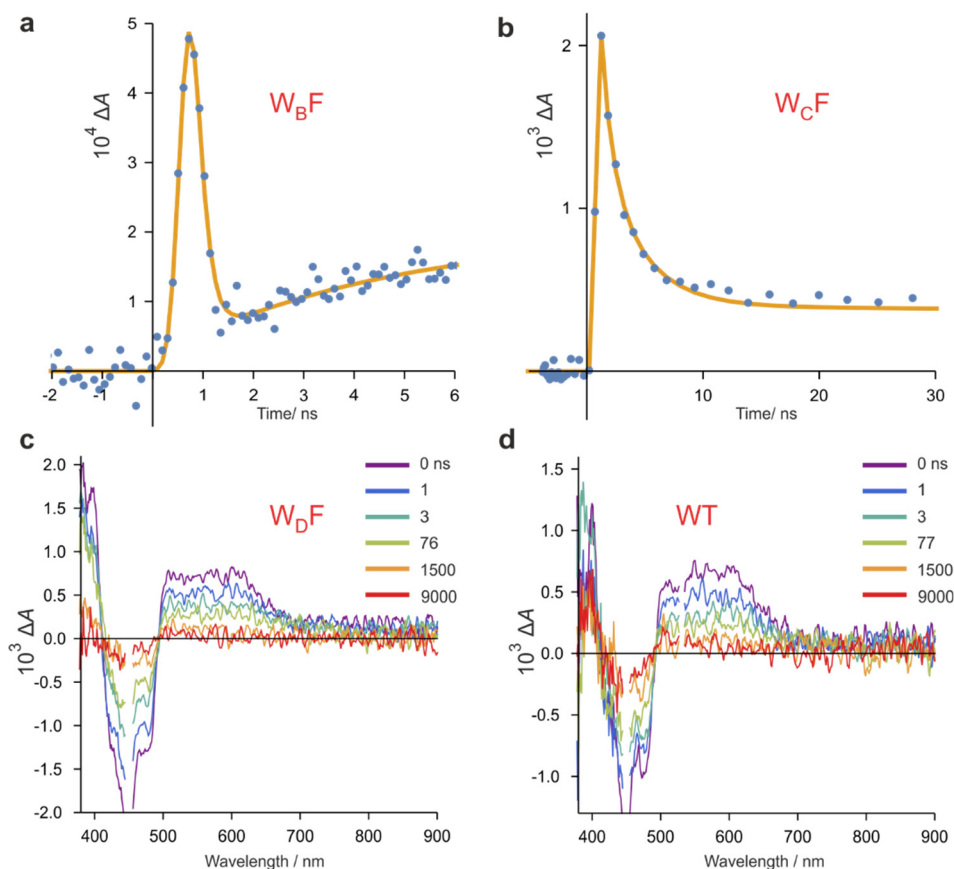


Fig. S2. Transient absorption kinetics and spectra of *ErCry4* WT and mutants.

a and **b**, Kinetic traces of $W_B F$ and $W_C F$ (blue), respectively, with tri-exponential fits (yellow). The time constants associated with loss of the radical signals are 180 ps and 900 ps, respectively. The TA data were averaged over the wavelength ranges 543 ± 15 nm and 514 ± 15 nm, respectively. The radical signal in **a** is superimposed on a signal from $^1FAD^*$, the excited triplet state of FAD (see Fig. S5). Experimental conditions: 50-60 μM protein in 20 mM Tris buffer with 200 mM NaCl, pH 8.0, with 20% glycerol and 1 mM $K_3Fe(CN)_6$ at 5 °C. Pump wavelength 450 nm. Representative ΔA spectra of the species FAD^{ox} , $FAD^{\bullet-}$, $FADH^{\bullet}$, $TrpH^{\bullet+}$, and Trp^{\bullet} can be found in Refs ^{12,72,73}.

c and **d**, Transient absorption spectra of *ErCry4* $W_B F$ and WT, respectively, at the indicated pump-probe delay times (in ns). The spectra are consistent with FAD and Trp radicals persisting for more than 10 μs . No other species are present on this timescale. The signals at ca. 450 nm were distorted by scattering of the pump light and have been removed. Experimental conditions: as for **a** and **b**, except that the proteins were purified using β -mercaptoethanol (BME) to prevent oligomerisation and to avoid problems with $^1FAD^*$. Prior to the measurements, BME was removed by washing with buffer solution. Approximately 1.5 mM $K_3Fe(CN)_6$ was then added to oxidise partially reduced protein ($FADH^{\bullet}$) and any remaining BME. A final wash with buffer removed Fe(II) and Fe(III). Fe(III) was then added to a concentration of 1 mM.

Comparison of magnetic field effects for *ErCry4* variants

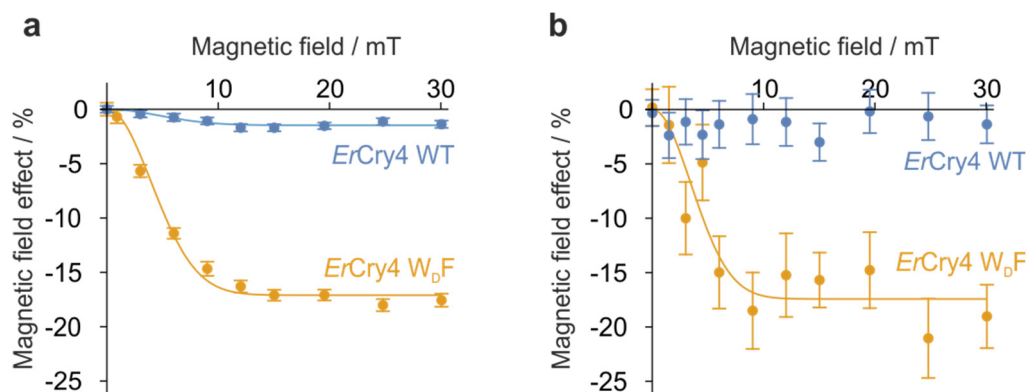


Fig. S3. Comparison of magnetic field effects for *ErCry4* variants.

a and **b**, Magnetic field effects on *ErCry4* WT and *ErCry4* W_DF at pH 7 recorded by CRDS.

a, Data from Fig. 2a and Fig. 2b, respectively, obtained from variants of the proteins with minor sequence errors close to the C-termini (see Methods for details). The data are presented as mean values \pm SEM (standard error of the mean) and the lines are Lorentzian fits to the data. See Statistics and Reproducibility information for Fig. 2a and 2b for further details.

b, Data obtained from samples of the two proteins with the correct sequences. The data are presented as mean values \pm SEM (standard error of the mean) and the line is a Lorentzian fit to the W_DF data.

The WT data are averages of 20 measurements on a single protein sample. Reproducibility was checked with two independently produced samples with comparable results. The W_DF data are averages of 20 measurements on a single protein sample. Reproducibility was checked with 2 independently produced samples with comparable results.

Within the experimental noise level, the sequence differences had no effect on the magnetic sensitivity. After the data in **a** were recorded, the apparatus used to acquire them was re-designed and re-built. The data in **b** were acquired with the new apparatus at a stage when its detection sensitivity had not been fully optimised.

Rate constants of the reactions of the RP_C/RP_D composite radical pair

The spin dynamics of the two rapidly interconverting states, RP_C and RP_D (Fig. 4a), can be simulated by means of a single radical pair with properties that are weighted averages of the properties of RP_C and RP_D, with weights f_C and $f_D = 1 - f_C$. The average rate constants for (spin-selective) singlet recombination and (non-selective) forward reaction (TrpH^{•+} deprotonation) are, respectively,

$$\begin{aligned}\langle k_r \rangle &= f_C k_{Cr} + (1 - f_C) k_{Dr} \\ \langle k_f \rangle &= f_C k_{Cf} + (1 - f_C) k_{Df}.\end{aligned}$$

k_{Cr} and k_{Dr} are the singlet recombination rate constants for RP_C and RP_D. k_{Cf} and k_{Df} are the rate constants for TrpH^{•+} deprotonation in RP_C and RP_D. Fig. 4a includes the reaction steps corresponding to each of these rate constants.

An approximate expression for the lifetime of the composite radical pair is

$$\left(\frac{1}{4} \langle k_r \rangle + \langle k_f \rangle \right)^{-1}$$

where the factor of $\frac{1}{4}$ accounts for the average probability that the radical pair is in a singlet state. Similarly, the lifetime of RP_C in the W_DF mutant is:

$$\left(\frac{1}{4} k_{Cr} + k_{Cf} \right)^{-1}.$$

The TA measurements show that a significant fraction of the photo-induced radicals in both the WT and W_DF proteins decays with a lifetime on the order of 100 ns. We interpret this as the lifetime of the composite radical pair in *ErCry4* WT and of RP_C in W_DF. Therefore:

$$\left(\frac{1}{4} \langle k_r \rangle + \langle k_f \rangle \right) \approx \left(\frac{1}{4} k_{Cr} + k_{Cf} \right) \approx \left(\frac{1}{4} k_{Dr} + k_{Df} \right) \approx 1.0 \times 10^7 \text{ s}^{-1}.$$

For radical pairs with lifetimes in the range 10 ns–10 μ s, simulations (Fig. 4b and 4c) show that the magnetic field effect is at a maximum when the singlet recombination rate constant is approximately three times the rate constant of the forward reaction. Since the magnetic field effect on the RP_C state of the mutant is large, we assume that $k_{Cr} / k_{Cf} \approx 3$. Combining this with $(\frac{1}{4} k_{Cr} + k_{Cf}) = 1.0 \times 10^7 \text{ s}^{-1}$ gives

$$k_{Cr} = 1.7 \times 10^7 \text{ s}^{-1} \quad \text{and} \quad k_{Cf} = 5.7 \times 10^6 \text{ s}^{-1}.$$

This rough estimate of k_{Cr} is consistent with the value derived from MD simulations: $(1.2 \pm 0.5) \times 10^7 \text{ s}^{-1}$ (Table S3).

For RP_D, we assume that the separation of the radicals is large enough that the recombination rate constant is effectively zero, so that

$$k_{Dr} = 0 \quad \text{and} \quad k_{Df} = 1.0 \times 10^7 \text{ s}^{-1}.$$

Taking $f_C = 0.1$, for example, so that the equilibrium ratio of RP_D to RP_C is 9:1, we obtain the weighted average rate constants:

$$\langle k_r \rangle = 1.7 \times 10^6 \text{ s}^{-1} \quad \text{and} \quad \langle k_f \rangle = 9.6 \times 10^6 \text{ s}^{-1}.$$

$\langle k_r \rangle / \langle k_f \rangle = 0.18$ is ~ 20 times smaller than required for strong magnetic sensitivity, i.e. $k_{Cr} / k_{Cf} = 3$. The composite radical pair should therefore show a much smaller magnetic field effect than RP_C in the W_{DF} mutant. This was confirmed by spin dynamics simulations (Fig. 4b).

In summary, the above values of k_{Cr} , k_{Cf} , k_{Dr} , and k_{Df} together with $f_C = 0.1$ can account for the similar (~ 100 ns) lifetimes of radicals in the WT and TrpD mutant proteins and the much larger magnetic field effect observed for W_{DF} *ErCry4* compared to WT *ErCry4*.

Simulation of OOP-ESEEM data

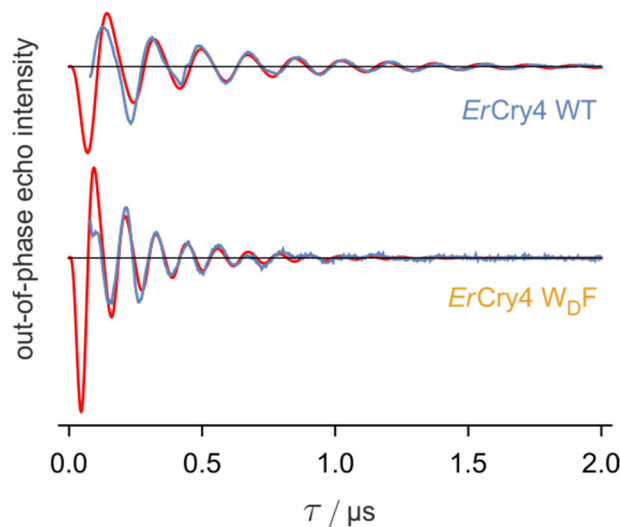


Fig. S4. Simulation of OOP-ESEEM data

The out-of-phase electron spin echo envelope modulation data Fig. 3b (blue) were simulated (red) using the following expression for the dependence of the echo intensity on the spin echo delay time, τ (Ref. ⁷⁴).

$$S(\tau) \propto \frac{\exp(-\tau/T)}{\sqrt{\tau}} \left[\sin\left(\frac{4\pi(D+3J)\tau}{3}\right) \text{FrC}(\sqrt{8D\tau}) - \cos\left(\frac{4\pi(D+3J)\tau}{3}\right) \text{FrS}(\sqrt{8D\tau}) \right],$$

where D and J are the magnitudes of the dipolar and exchange interactions (expressed as frequencies), T is the relaxation time and the Fresnel functions are :

$$\text{FrC}(z) = \int_0^z \cos\left(\frac{\pi u^2}{2}\right) du \quad \text{FrS}(z) = \int_0^z \sin\left(\frac{\pi u^2}{2}\right) du .$$

Nuclear ESEEM modulations were not included.

Satisfactory simulations of the experimental data (recorded for $80 \text{ ns} < \tau < 2 \mu\text{s}$) were obtained with the following parameters:

$$\text{ErCry4 WT: } D = -8.70 \text{ MHz}, J = 0.02 \text{ MHz}, T = 0.75 \mu\text{s}.$$

$$\text{ErCry4 W}_D\text{F: } D = -13.20 \text{ MHz}, J = 0.05 \text{ MHz}, T = 0.35 \mu\text{s}.$$

Fig. S4 shows the data (blue, also in Fig. 3b) together with this simulation (red).

The mean distances between the centres of gravity of the aromatic rings of the $\text{FAD}^{\bullet-}$ and $\text{TrpH}^{\bullet+}$ radicals in the two radical pairs, obtained from the MD simulations (Table S2), are

$$r(\text{RP}_D) = 2.16 \text{ nm} \text{ and } r(\text{RP}_C) = 1.85 \text{ nm}.$$

The corresponding distances for FAD and TrpH in the crystal structure of pigeon Cry4¹⁵ are

$$r(\text{RP}_\text{D}) = 2.13 \text{ nm} \text{ and } r(\text{RP}_\text{C}) = 1.76 \text{ nm}.$$

Using a point-dipole approximation, the dipolar coupling is related to the separation between the radicals, r , by

$$D/\text{MHz} = \frac{-77.98}{(r/\text{nm})^3}.$$

The values of D obtained from the OOP-ESEEM simulation give radical-radical separations

$$r(\text{WT}) = 2.1 \text{ nm} \text{ and } r(\text{W}_\text{D}\text{F}) = 1.8 \text{ nm}.$$

$r(\text{W}_\text{D}\text{F})$ is consistent with $r(\text{RP}_\text{C})$, as expected when electron transfer beyond Trp_C is blocked.

$r(\text{WT})$ is compatible with $r(\text{RP}_\text{D})$, and would not be inconsistent with a composite $\text{RP}_\text{C}/\text{RP}_\text{D}$ radical pair in which RP_C was a minor (e.g. 10%) contributor.

To investigate whether an equilibrium between RP_C and RP_D exists under the conditions of the OOP-ESEEM experiments, we measured the temperature dependence of the signal. No change was observed when the temperature was raised from 80 K to 200 K.

The custom code used to simulate the OOP-ESEEM signals (Wolfram Mathematica 12) is available at: http://hore.chem.ox.ac.uk/Nature_2021/Codes.zip.

Spectra of $^5\text{FAD}^*$ and $^T\text{FAD}^*$

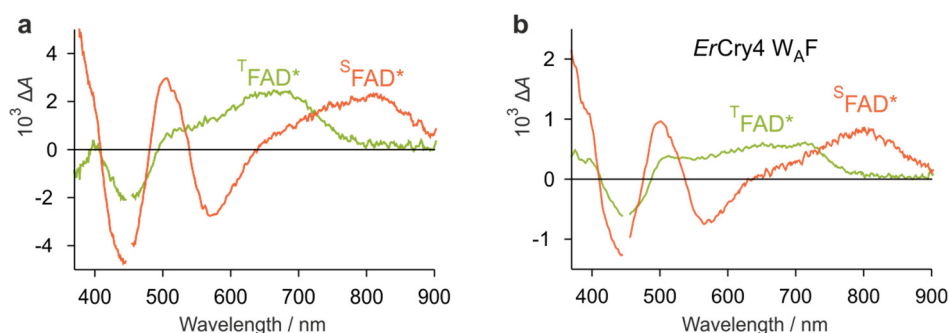


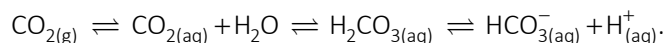
Fig. S5. Spectra of $^5\text{FAD}^*$ and $^T\text{FAD}^*$.

a, Transient absorption spectra of free FAD recorded with pump-probe delays of 1.2 ns ($^5\text{FAD}^*$, red) and 20 ns ($^T\text{FAD}^*$, green). These spectra were recorded to confirm the identity of the signals observed for *ErCry4* WT (shown in **b**).

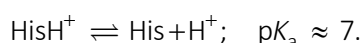
b, Some of our early transient absorption experiments were performed on protein samples that had been purified without β -mercaptoethanol (Fig. S2a and S2b) and which consequently were partially oligomerised via disulphide links. Fig. S5b shows TA spectra of *ErCry4* $\text{W}_\text{A}\text{F}$ obtained from global analysis of the raw data by applying a target model of the sequential reaction steps ($^5\text{FAD}^* \rightarrow ^T\text{FAD}^* \rightarrow \text{FAD}^{\text{ox}}$) using a Matlab-based toolbox⁷⁵. The Species Associated Difference Spectra reveal the spectra of two distinct species, decaying with time constants of 4.27 ns ($^5\text{FAD}^*$) and 1.15 μs ($^T\text{FAD}^*$). It appears that, under the conditions of these experiments, a proportion of the *ErCry4* WT molecules do not undergo photo-induced electron transfer, but instead form these transient excited states. We presume that subtle differences in the folding of these molecules, induced by oligomerisation, inhibit electron transfer from Trp_A to $^5\text{FAD}^*$, allowing $^T\text{FAD}^*$ to be formed. Apart from reducing the yield of radical pairs (and therefore the spectral signal-to-noise), and obscuring the spectra of the FAD and Trp radicals at pump-probe times less than ca. 1 μs , this unproductive side-reaction had no effect on the results or conclusions presented here. Later TA measurements (Fig. 3c, S2c, and S2d) were all recorded using samples of monomeric proteins purified using BME.

Choice of pH 8 for spectroscopic measurements at 5 °C

The typical physiological conditions inside an avian cell are 40-43 °C and pH \approx 7.3, the pH being regulated by the carbonate/bicarbonate buffer system:



Many studies (reviewed by Reeves³⁷ and by Roos and Boron³⁶) have shown that intracellular pH rises when the temperature drops in such a way as to maintain the net charge states of proteins. The argument goes as follows. In the physiological pH range (pH 6-8), the only titratable groups in proteins are the imidazole side-chains of histidine residues:



The enthalpy of ionisation of histidine is ca. 20 kJ mol⁻¹ (Nagai *et al.*⁷⁶), resulting in an increase in the pK_a of the imidazole group of ca. 0.7 when the temperature is reduced from 40-43 °C to 5 °C (the temperature of our spectroscopic measurements*). If this change is offset by an equal increase in pH, the histidine acid-base balance will be preserved:

$$K_a = \frac{[\text{His}][\text{H}^+]}{[\text{HisH}^+]} \Rightarrow \log_{10} \left\{ \frac{[\text{His}]}{[\text{HisH}^+]} \right\} = -\text{p}K_a + \text{pH}$$

We have therefore chosen to perform most of our spectroscopic measurements at pH 7.3 + 0.7 = 8.0 where proteins should have the same overall charge as at physiological temperature and pH.

*Lowering the temperature and addition of glycerol were found to enhance the magnetic field effects.

ErCry4 stability in MD simulations

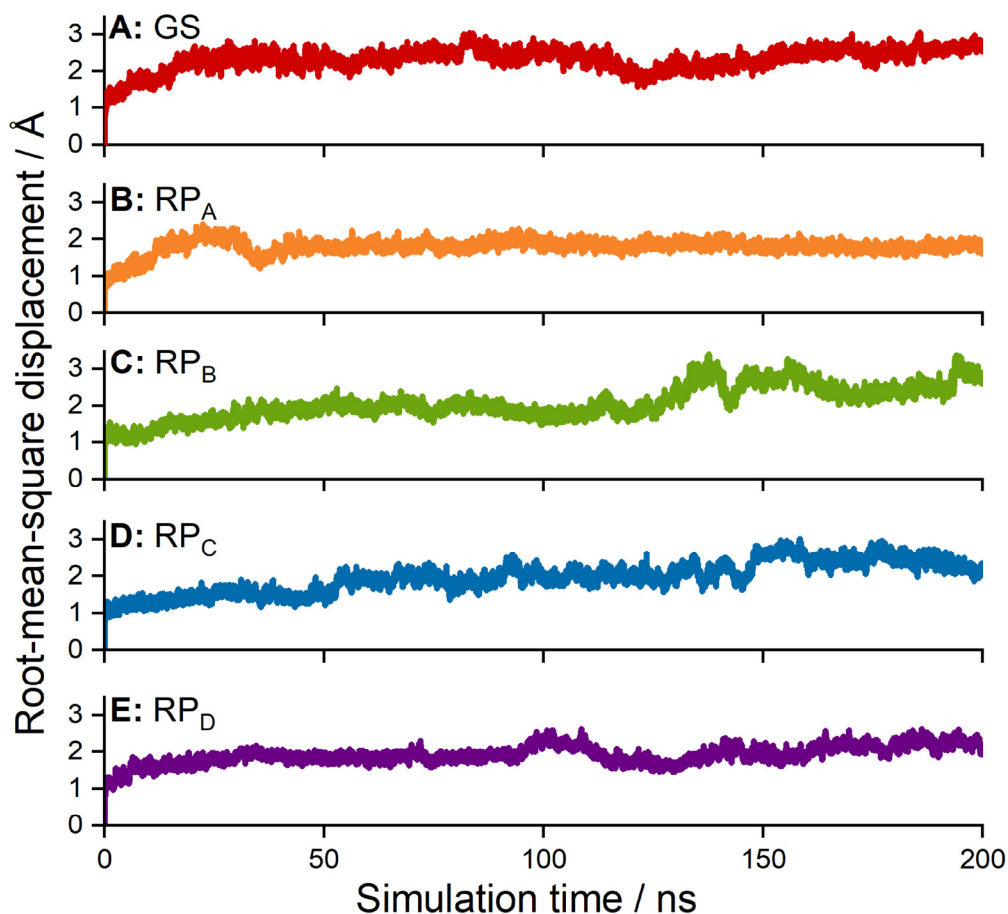


Fig. S6. Stability of the *ErCry4* structural models.

Root-mean-square displacement (RMSD) computed for the backbone atoms of *ErCry4* in the course of production simulations of the *ErCry4* models in different redox states. The RMSD was computed using Eqn (S.1) relative to the structure obtained after equilibration (Table M2). Simulated MD trajectories from which the data shown here were obtained are available upon request. Simulation input files may be downloaded from the simulation files subfolder of the simulation data archive. Analysis was carried out using VMD 1.9.3⁶¹.

An important measure for molecular system stability analysis is the root-mean-square displacement (RMSD), which indicates how much the atoms in a molecular structure are displaced on average compared to a reference position. The RMSD is defined as:

$$RMSD = \sqrt{\frac{\sum_{i=1}^N [\mathbf{r}_i(t_{\text{ref}}) - \mathbf{r}_i(t)]^2}{N}} \quad (\text{S.15})$$

where N is the total number of atoms in the structure, and $\mathbf{r}_i(t_{\text{ref}})$ and $\mathbf{r}_i(t)$ denote the positions of an atom i at times t_{ref} and t .

Edge-to-edge distances

	Edge-to-edge distance / nm				
	GS	RP _A	RP _B	RP _C	RP _D
FAD-Trp _A	0.38±0.03	0.39±0.03	0.39±0.03	0.39±0.03	0.39±0.03
FAD-Trp _B	0.85±0.04	0.85±0.03	0.89±0.04	0.88±0.04	0.90±0.03
FAD-Trp _C	1.28±0.04	1.29±0.03	1.30±0.04	1.33±0.04	1.31±0.04
FAD-Trp _D	1.60±0.04	1.60±0.03	1.59±0.04	1.58±0.04	1.60±0.04
Trp _A -Trp _B	0.39±0.02	0.37±0.02	0.41±0.03	0.40±0.02	0.40±0.02
Trp _B -Trp _C	0.41±0.04	0.41±0.04	0.37±0.03	0.45±0.04	0.41±0.04
Trp _C -Trp _D	0.36±0.02	0.37±0.02	0.37±0.02	0.36±0.02	0.36±0.02
Trp _D -Tyr319	0.37±0.02	0.38±0.02	0.38±0.02	0.41±0.03	0.38±0.03

Table S1. Edge-to-edge distances in *ErCry4*.

Edge-to-edge distances between the FAD and the four tryptophans, between neighbouring tryptophans, and from Trp_D to Tyr319 for each of the five redox states of *ErCry4*. The edge-to-edge distance between two groups is the shortest distance between the carbon or nitrogen atoms in the aromatic ring systems. The results were obtained by sampling the 200 ns production MD simulations. The mean value corresponds to the most probable distance and the error is computed as the standard deviation. Simulated MD trajectories from which the data shown here were obtained are available upon request. Simulation input files may be downloaded from the simulation files subfolder of the simulation data archive. Tables with the computed distances are available in the distances_contact subfolder of the simulation data archive. Analysis was carried out using VMD 1.9.3⁶¹.

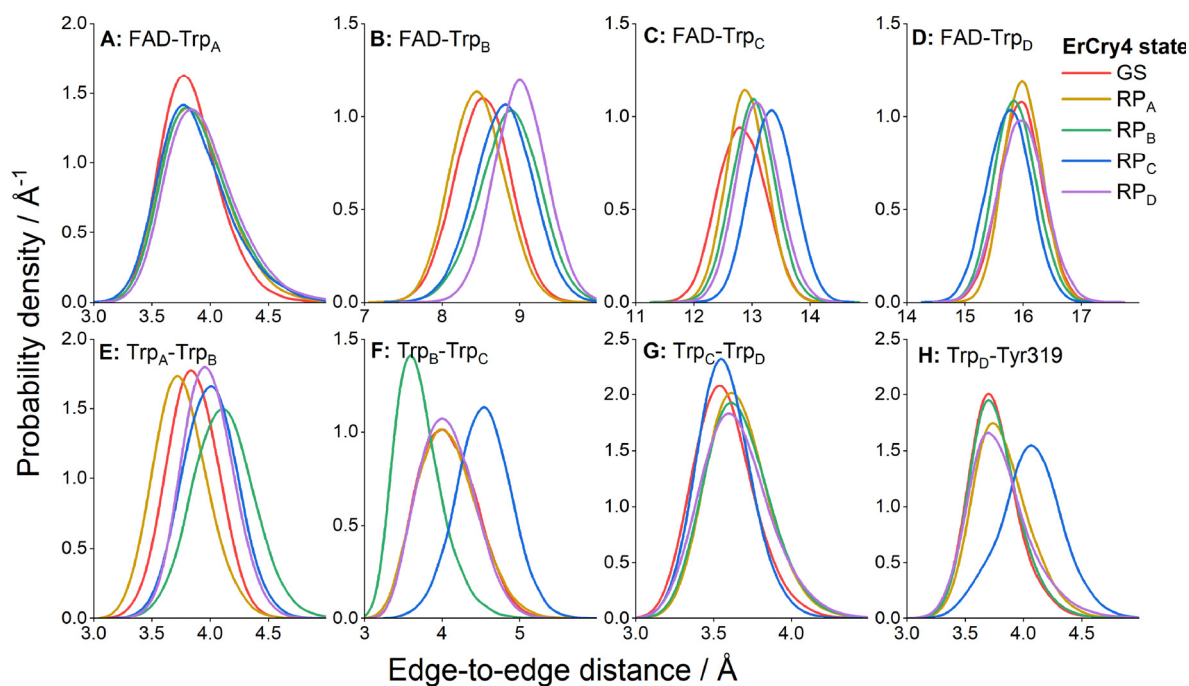


Fig. S7. Probability density distributions for the edge-to-edge distances in *ErCry4*.

Distributions were computed for *ErCry4* in five redox states. These distributions were used to obtain the data in [Table S1](#). The plots represent data recorded during the 200 ns long production MD simulations. The sampling interval was equal to 5 ps. Simulated MD trajectories from which the data shown here were obtained are available upon request. Simulation input files may be downloaded from the simulation files subfolder of the simulation data archive. Tables with the computed distances are available in the distances_contact subfolder of the simulation data archive. Analysis was carried out using VMD 1.9.3⁶¹.

Centre-to-centre distances

	Centre-to-centre distance / nm				
	GS	RP _A	RP _B	RP _C	RP _D
FAD-Trp _A	0.83±0.03	0.82±0.02	0.81±0.03	0.81±0.03	0.86±0.03
FAD-Trp _B	1.31±0.03	1.30±0.04	1.35±0.04	1.30±0.03	1.33±0.03
FAD-Trp _C	1.81±0.04	1.82±0.03	1.81±0.03	1.85±0.03	1.84±0.03
FAD-Trp _D	2.17±0.04	2.16±0.03	2.14±0.03	2.14±0.04	2.16±0.04
Trp _A -Trp _B	0.70±0.03	0.67±0.04	0.73±0.04	0.72±0.03	0.72±0.03
Trp _B -Trp _C	0.73±0.04	0.73±0.04	0.68±0.03	0.78±0.03	0.73±0.04
Trp _C -Trp _D	0.51±0.02	0.52±0.02	0.52±0.02	0.52±0.02	0.53±0.02
Trp _D -Tyr319	0.62±0.06	0.66±0.11	0.62±0.08	0.80±0.11	0.63±0.09

Table S2. Centre-to-centre distances in *ErCry4*.

Same as [Table S1](#) except that the distances are calculated between the centres of mass of the aromatic ring systems. Simulated MD trajectories from which the data shown here were obtained are available upon request. Simulation input files may be downloaded from the simulation files subfolder of the simulation data archive. Tables with the computed distances are available in the distances_COM subfolder of the simulation data archive. Analysis was carried out using VMD 1.9.3⁶¹.

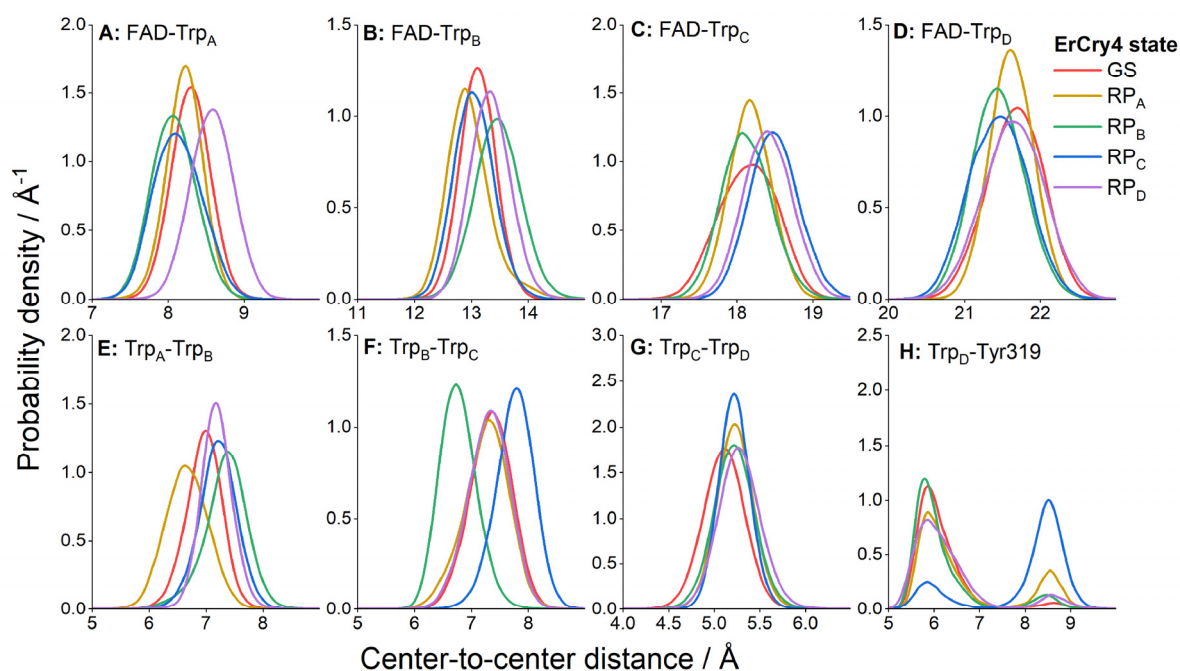


Fig. S8. Probability density distributions for the centre-to-centre distances in *ErCry4*.

Distributions were computed for *ErCry4* in five redox states. These distributions were used to obtain the data in Table S2. The distribution for Trp_D-Tyr319, in particular for the RP_C state, arises from movement of the sidechain of Y319 between two positions ~ 3.5 \AA apart. Simulated MD trajectories from which the data shown here were obtained are available upon request. Simulation input files may be downloaded from the simulation files subfolder of the simulation data archive. Tables with the computed distances are available in the distances_COM subfolder of the simulation data archive. Analysis was carried out using VMD 1.9.3⁶¹.

Electron transfer rate constants

	Energy / kcal mol ⁻¹		Edge-to-edge distance / Å	Electron transfer rate constant / s ⁻¹
	λ	ΔG	R	k
RP _A → RP _B	17.7±0.2	-5.814±0.006	3.7±0.2	(7.4±1.8) × 10 ¹¹
RP _B → RP _A	28.7±0.7	5.814±0.006	4.1±0.3	(1.3±0.5) × 10 ⁷
RP _B → RP _C	30.8±0.3	-8.146±0.004	3.7±0.3	(5.0±1.8) × 10 ¹⁰
RP _C → RP _B	29.7±0.4	8.146±0.004	4.5±0.4	(9.0±4.1) × 10 ⁵
RP _C → RP _D	22.8±0.3	-0.717±0.004	3.6±0.2	(1.3±0.4) × 10 ¹⁰
RP _D → RP _C	19.5±0.2	0.717±0.004	3.6±0.2	(1.5±0.4) × 10 ¹⁰
RP _C → GS	46.5±0.6	-41.392±0.003	13.3±0.4	(1.2±0.5) × 10 ⁷
RP _D → GS	41.3±0.5	-38.579±0.004	16.0±0.4	(3.4±1.5) × 10 ⁵

Table S3. Electron transfer rate constants in *ErCry4*.

The electron transfer rate constants, k , for the different electron transfers in *ErCry4* were computed using Eqn M14 based on the values of the reorganisation energy λ , the driving force ΔG the electron donor-acceptor distance R . The changes of *ErCry4* redox state are indicated in the first column, the values of R were taken from Table S1, the values of λ and ΔG were computed from Fig. S9 and S10. Note that the values of R for the direct and reverse electron transfer processes may be different as the protein structure adapts to the change of the redox state in the active site. An error analysis was carried out for λ , ΔG and R based on the data obtained from the MD simulations and shown in Fig. S7, S9, and S10. These errors were used to estimate the uncertainties in the values of the electron transfer rate constants, k . Given the nature of the approximations involved in obtaining these rate constants, we regard them as order of magnitude estimates. Simulated MD trajectories from which the data shown here were obtained are available upon request. Simulation input files may be downloaded from the simulation files subfolder of the simulation data archive. Tables with the computed energies as well as the custom-made tcl scripts used to obtain these values from the simulated trajectories are available in the energies subfolder of the simulation data archive. Analysis was carried out using VMD 1.9.3⁶¹.

snapshot	$E(\text{FAD}) /$ Hartree	$E(\text{FAD}^{\bullet-}) /$ Hartree	$E(\text{TrpH}) /$ Hartree	$E(\text{TrpH}^{\bullet+}) /$ Hartree
1	-3348.876145	-3348.847369	-610.490577	-610.220191
2	-3348.896486	-3348.865900	-610.483527	-610.212262
3	-3348.926971	-3348.886645	-610.498375	-610.235636
4	-3348.899618	-3348.869762	-610.489765	-610.230447
5	-3348.914049	-3348.879728	-610.470099	-610.214302
6	-3348.969747	-3348.926597	-610.511500	-610.251803
7	-3348.922615	-3348.882556	-610.500838	-610.236486
8	-3348.944825	-3348.901482	-610.475572	-610.222697
9	-3348.948016	-3348.913613	-610.495564	-610.229684
10	-3348.917815	-3348.889994	-610.502767	-610.240836
11	-3348.949902	-3348.907877	-610.502788	-610.231679
12	-3348.870066	-3348.829760	-610.497181	-610.229287
13	-3348.903743	-3348.866857	-610.481112	-610.215702
14	-3348.930927	-3348.893213	-610.502829	-610.237990
15	-3348.982143	-3348.944909	-610.510677	-610.247181
16	-3348.966627	-3348.932901	-610.482468	-610.216405
17	-3348.921128	-3348.888187	-610.471694	-610.212996
18	-3348.895084	-3348.859063	-610.479169	-610.214836
19	-3348.951877	-3348.915191	-610.503033	-610.245704
20	-3348.851367	-3348.812326	-610.475559	-610.208687
Mean value	-3348.921958	-3348.885696	-610.491255	-610.227740

Table S4. Self-energies of *ErCry4* cofactors involved in electron transfers.

The representative self-energies of the redox cofactors FAD, $\text{FAD}^{\bullet-}$, TrpH, and $\text{TrpH}^{\bullet+}$ were computed using the CAM-B3LYP/6-31G method for 20 *ErCry4* randomly selected snapshots from a completed MD simulation of *ErCry4* GS. Input and output files for the considered structures are available in the QM_energies subfolder of the simulation data archive. Computations were carried out using Gaussian 09⁶³.

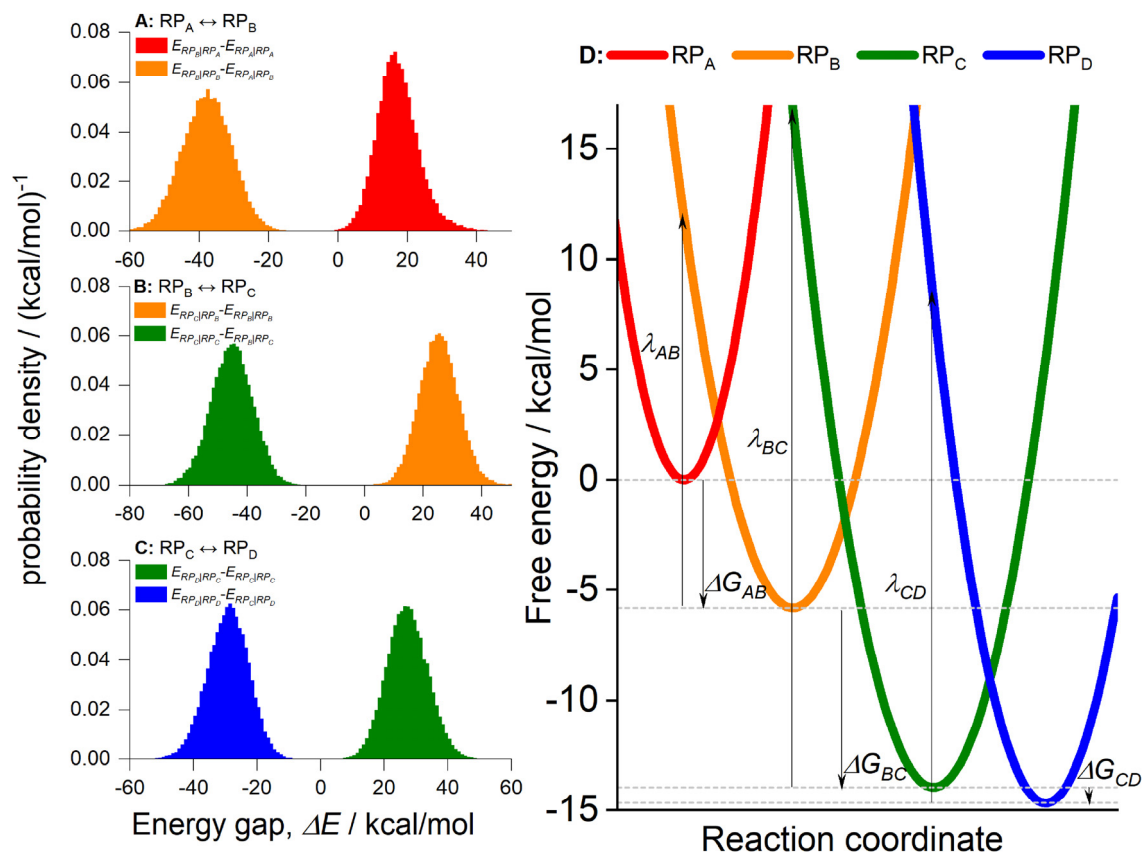


Fig. S9. Free energy profiles for the radical pair states in *ErCry4*.

Probability density distributions of the energy gaps ΔE_{react} and ΔE_{prod} calculated using Eqns M10 and M11 for the $RP_A \leftrightarrow RP_B$ (A), $RP_B \leftrightarrow RP_C$ (B) and $RP_C \leftrightarrow RP_D$ (C) electron transfer processes. The distributions were used to plot the free energies of the different redox states in *ErCry4* (D), following Eqn M13. The key reorganisation energies λ and driving forces ΔG are indicated. Simulated MD trajectories from which the data shown here were obtained are available upon request. Simulation input files may be downloaded from the simulation files subfolder of the simulation data archive. Tables with the computed energies as well as the custom-made tcl scripts used to obtain these values from the simulated trajectories are available in the energies subfolder of the simulation data archive. Analysis was carried out using VMD 1.9.3.

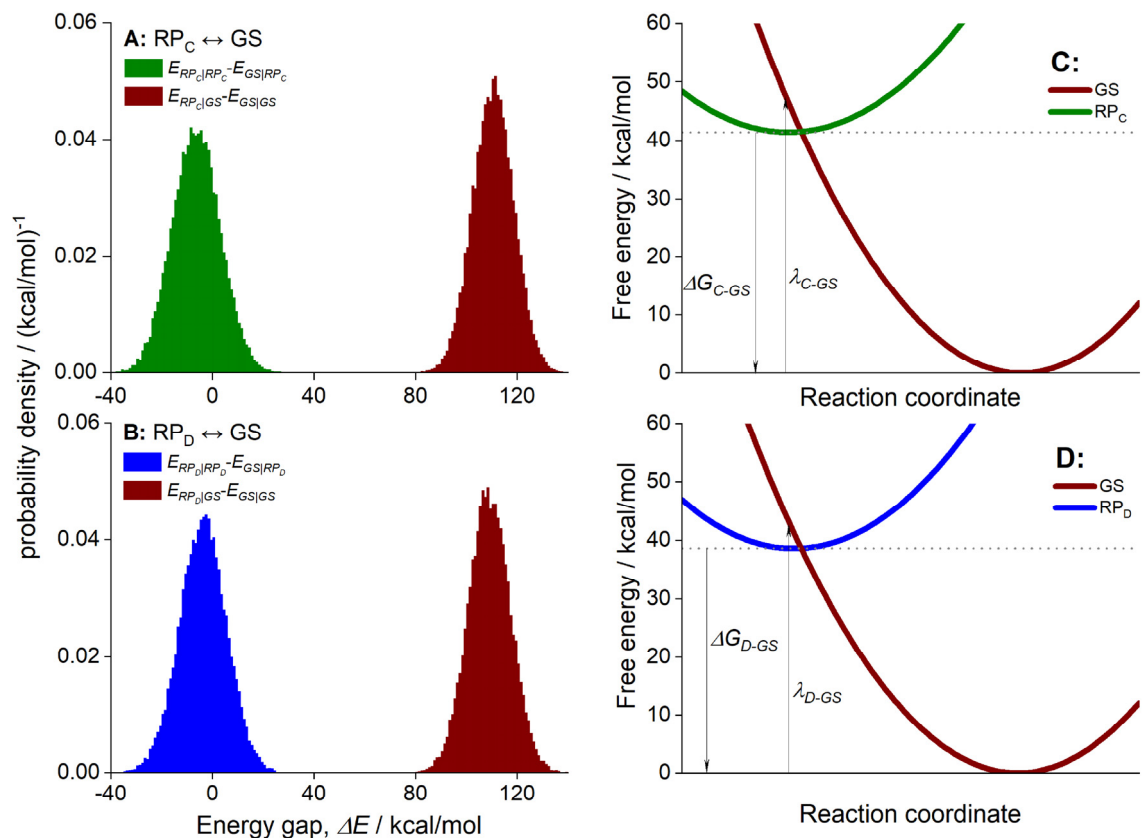


Fig. S10. Free energy profiles for recombination reactions in *ErCry4*.

The figure is similar to Fig. S9, but shows the probability density distributions of the energy gaps ΔE_{react} and ΔE_{prod} calculated using Eqns M10 and M11 for the recombination reactions $RP_C \leftrightarrow GS$ (A) and $RP_D \leftrightarrow GS$ (B). The corresponding free energy profiles are shown in C and D. The key reorganisation energies λ and driving forces ΔG are indicated. Simulated MD trajectories from which the data shown here were obtained are available upon request. Simulation input files may be downloaded from the simulation files subfolder of the simulation data archive. Tables with the computed energies as well as the custom-made tcl scripts used to obtain these values from the simulated trajectories are available in the energies subfolder of the simulation data archive. Analysis was carried out using VMD 1.9.3.

Hydrogen bonding network

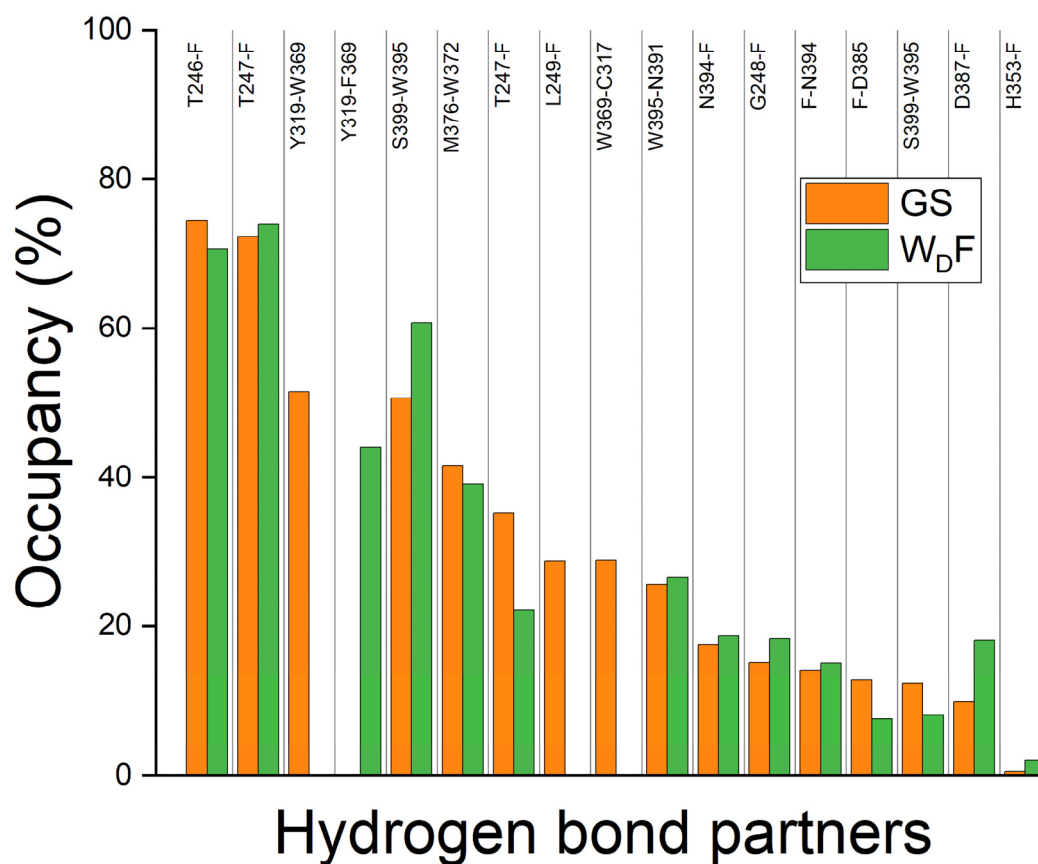


Fig. S11. Hydrogen bonding network in *ErCry4*.

The figure shows the fractions of the simulation time (the occupancy) for which specific hydrogen bonds exist in the GS and W_DF simulations of *ErCry4*. Hydrogen bonds are considered between the rest of the protein and the FAD cofactor, Trp_A, Trp_B, Trp_C and Trp_D in the case of the GS simulation and the FAD cofactor, Trp_A, Trp_B, Trp_C and F369 in the case of the W_DF simulation. Simulated MD trajectories from which the data shown here were obtained are available upon request. Simulation input files may be downloaded from the simulation files subfolder of the simulation data archive. Analysis was carried out using VMD 1.9.3⁶¹.

Radical pair kinetics from transient absorption measurements

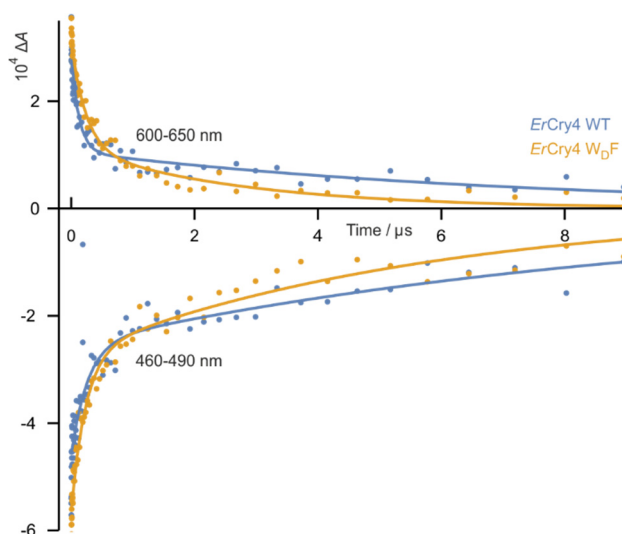


Fig. S12. Time-dependence of radical concentrations.

The data shown in Fig. 3c are taken from a set of measurements for pump-probe delays of 5 ns–9 μ s. On this timescale both proteins show biphasic kinetics at both wavelengths with time constants of ~ 100 ns and ~ 5 μ s. The solid lines are intended to guide the eye. We interpret the ~ 100 ns component as the lifetime of the composite radical pair in *ErCry4* WT and of RP_C in *W₅F*. It is less clear how to assign the ~ 5 μ s component. With electron spin relaxation rates probably in the range 100 ns to 1 μ s, it is too slow to make a significant contribution to the generation of magnetic field effects and may be related to the recombination of the stabilised radical pairs, $RP_{2X} = [FAD^{\bullet-} Trp_X^{\bullet}]$, X = C and D.

Incorporation of FAD in *ErCry4*

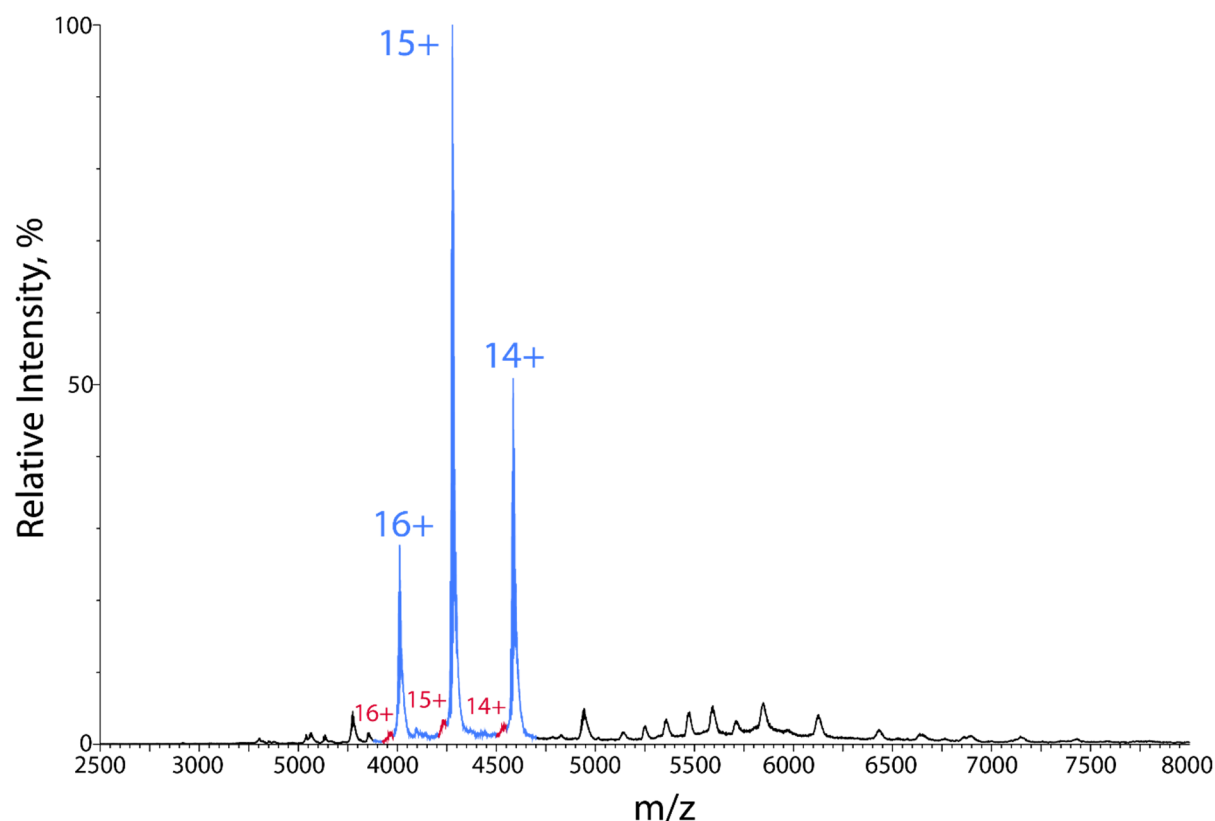


Fig. S13. Native mass spectrum of *ErCry4* wild-type.

Two charge-state series consistent with the monomer were detected: major peaks (blue) correspond to charge states of holo-*ErCry4* monomer (molecular mass 64.197 ± 29 kDa, > 97% abundance) and minor peaks (red) correspond to charge states of apo-*ErCry4* (molecular mass 63.430 ± 16 kDa, < 3% abundance). The mass difference between the two is approximately 767 Da, consistent with the FAD cofactor (785.5 Da). The differences between the detected masses and the expected masses (64.033 kDa for holo-*ErCry4*, 63.248 kDa for apo-*ErCry4*, both including the N-terminal tag) are due to salt ions and buffer components, in this case principally Na^+ . The peaks in the range $m/z = 5000$ -7000 arise from a small amount of dimerised protein. These measurements were performed on an Orbitrap Q Exactive Plus mass spectrometer (Thermo Scientific) modified for transmission of high mass species using nano-electrospray ionisation.

Photoreduction of *ErCry4* W_DF

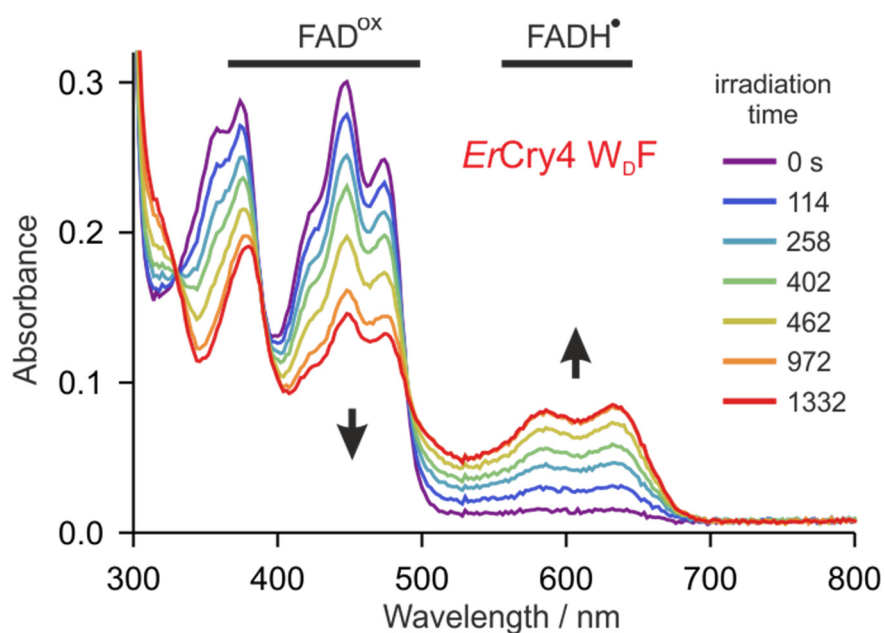


Fig. S14. Photoreduction of *ErCry4* W_DF by continuous irradiation at 450 nm.

UV-visible spectra show depletion of FAD^{ox} (400–500 nm) and accumulation of FADH[•] (500–700 nm). Experimental conditions: 30 μ M protein samples in 20 mM Tris buffer, pH 8.0, 5 mM dithiothreitol, with 20% glycerol at 5 °C. The shoulder at \sim 480 nm on the 450 nm peak is characteristic of correctly bound FAD^{ox}. Samples were irradiated using a 3.5 mW 450 nm LED ($260 \mu\text{mol m}^{-2} \text{s}^{-1} = 70 \text{ W m}^{-2}$).

Post-irradiation re-oxidation kinetics of *ErCry4* WT

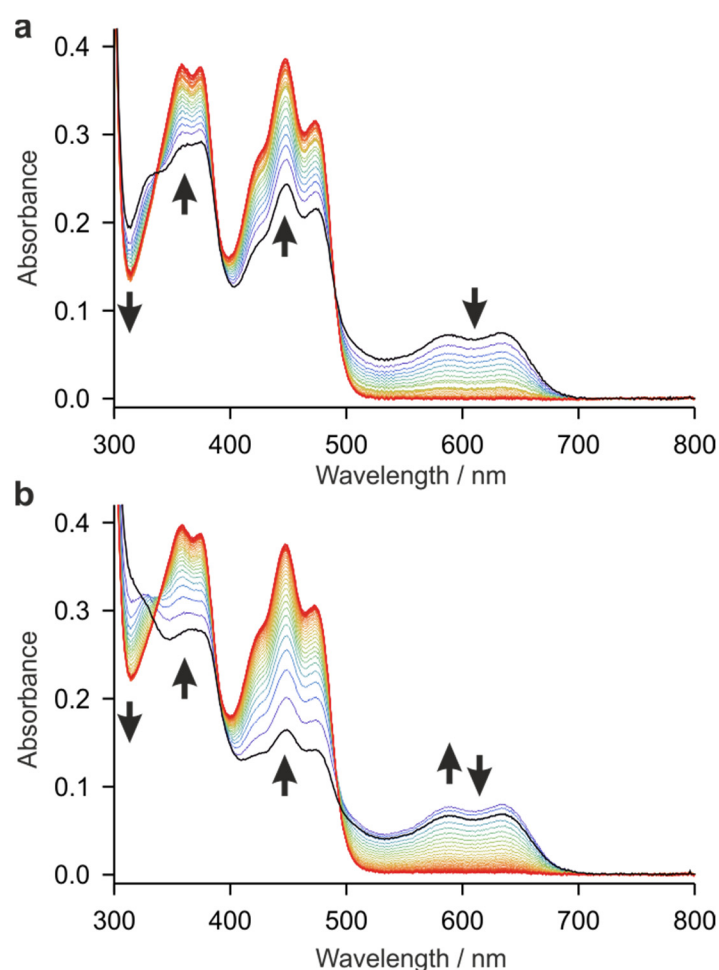


Fig. S15. Re-oxidation of photo-reduced *ErCry4* WT without added redox agents.

Time-dependence of the UV-vis spectrum of *ErCry4* WT under aerobic conditions after 2-min illumination at 450 nm with intensity (a) 260 $\mu\text{mol m}^{-2} \text{s}^{-1}$ ($= 70 \text{ W m}^{-2}$) and (b) 2,600 $\mu\text{mol m}^{-2} \text{s}^{-1}$ ($= 700 \text{ W m}^{-2}$). The spectra are at 2-min intervals from $t = 0$ (immediately after illumination, black) to $t = 78$ min (red). The recovery of the fully oxidised ground state of the protein, containing FAD^{ox} , is seen in the growth of the absorption at 400-500 nm. The disappearance of FADH^{\bullet} is responsible for the loss of absorption between 500 and 700 nm. The isosbestic points at ~ 330 nm, ~ 390 nm and ~ 490 nm in the low power experiment (a) shows that only two species are involved (assigned to FAD^{ox} and FADH^{\bullet} , see Fig. S17). The absence of the isosbestic point at ~ 330 nm in the first few spectra in the high power experiment (b) indicates the presence of a third species (assigned to the fully reduced state FADH^{-} , see Fig. S17). Experimental conditions: 35 μM protein in 20 mM Tris buffer, pH 8.0, 200 mM NaCl, with 20% glycerol at 20 $^{\circ}\text{C}$. No oxidants or reductants were present in the samples.

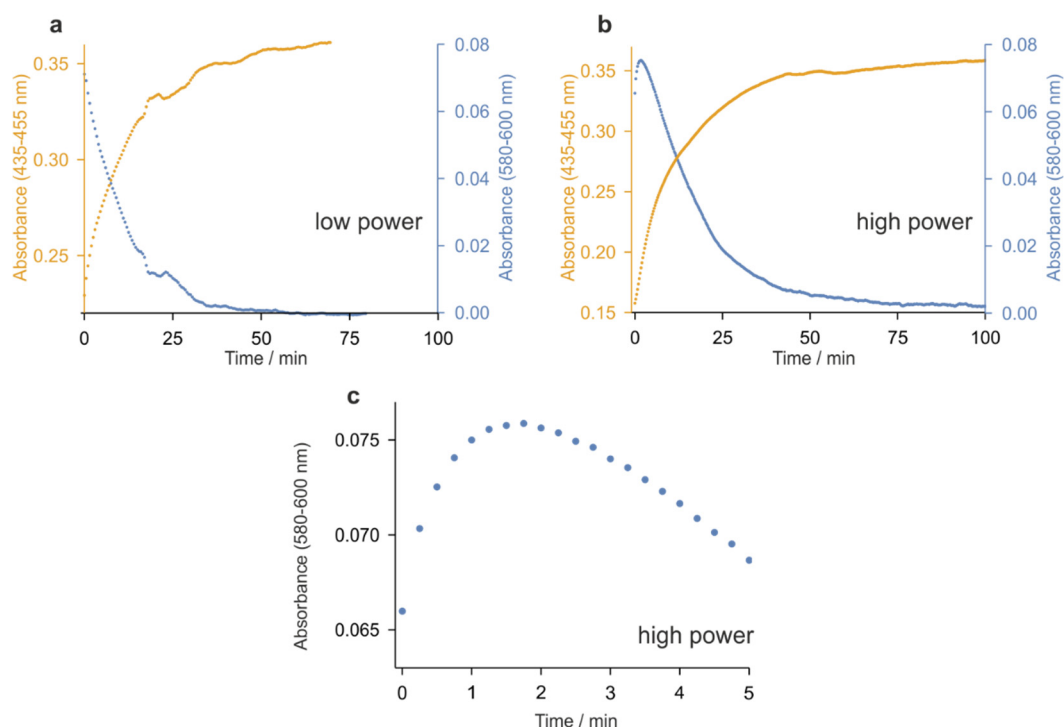


Fig. S16. Kinetics of re-oxidation of photo-reduced *ErCry4* WT without added redox agents.

Time-dependence of the absorbance of *ErCry4* WT solutions under aerobic conditions after 2-min illumination at 450 nm with intensity (a) $260 \mu\text{mol m}^{-2} \text{s}^{-1}$ and (b, c) $2,600 \mu\text{mol m}^{-2} \text{s}^{-1}$. The corresponding UV-vis spectra are shown in Fig. S15. (a) Conversion of FADH^+ to FAD^{ox} . (b, c) Conversion of FADH^- and FADH^\bullet to FAD^{ox} . (c) is an expanded view of the absorbance at 580-600 nm in the first 5 min after illumination. The initial rise in (c) is assigned to the oxidation of FADH^- to FADH^\bullet which then converts more slowly to FAD^{ox} (see Fig. S17). The growth of the signal at 435-455 nm in (a) and (b) reflects the recovery of the FAD^{ox} state. Experimental conditions: as for Fig. S15. No oxidants or reductants were added to the samples. Note the different vertical scales for the two wavelength bands in (a) and (b).

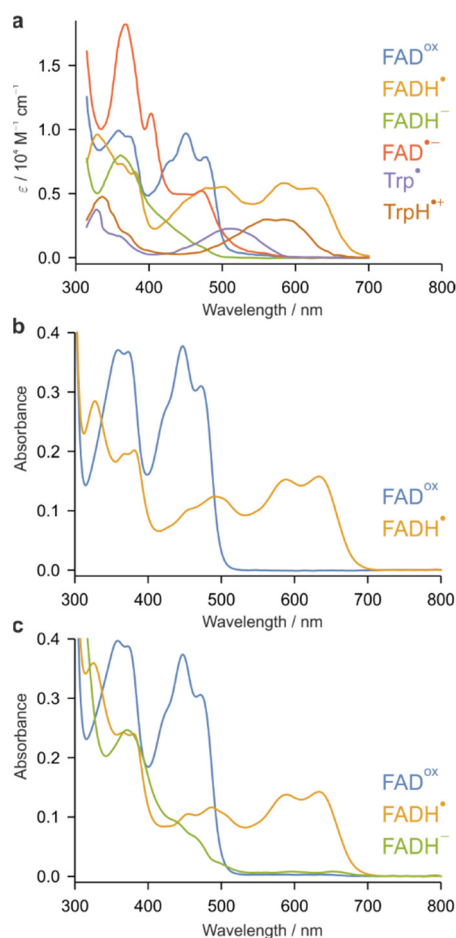
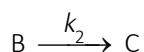


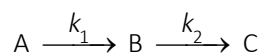
Fig. S17. Model spectra and species-associated spectra (SAS).

(a) Model spectra of key species: extinction coefficients as a function of wavelength. Spectra adapted from Liu *et al.*⁷² (FAD species) and Müller *et al.*⁷⁷ (Trp radicals).

(b, c) SAS obtained by global analysis (see Methods) of *ErCry4* WT data recorded after 2-min illumination at 450 nm with intensity (b) 260 $\mu\text{mol m}^{-2} \text{s}^{-1}$ and (c) 2,600 $\mu\text{mol m}^{-2} \text{s}^{-1}$. Kinetic models used in the analysis were:



for the lower power experiments and



for the high power experiments. k_1 and k_2 are first order rate constants. Comparison with the model spectra in (a) allowed A, B and C to be assigned to the FADH^- , FADH^\bullet , and FAD^{ox} states of *ErCry4*. We presume that FADH^- is formed by photoreduction of FADH^\bullet under high power illumination. No contribution from FADH^- was required to account for the data in the low power experiment. The rate constants and fractional concentrations of the three redox states of *ErCry4* are shown in Table S5.

	power	$(k_1)^{-1}/\text{min}$	$(k_2)^{-1}/\text{min}$	$[\text{FADH}^-]/\%$	$[\text{FADH}^\bullet]/\%$	$[\text{FAD}^{\text{ox}}]/\%$
<i>ErCry4</i> WT	low	—	12.7	—	47	53
	high	0.9	12.5	35	39	26
<i>ErCry4</i> W _D F	low	—	12.3	—	31	69
	high	0.8	12.8	27	40	33
<i>GgCry</i> WT	low	—	29.1	—	59	41
<i>ClCry</i> WT	low	—	3.6	—	39	61

Table S5. Global analysis of re-oxidation data without added redox agents.

Values of rate constants k_1 and k_2 and percentage initial concentrations obtained by global analysis (see Methods) of UV-vis spectra recorded after 2-min irradiation at 450 nm with intensity $260 \mu\text{mol m}^{-2} \text{s}^{-1}$ (low power) or $2,600 \mu\text{mol m}^{-2} \text{s}^{-1}$ (high power). For both robin *Cry4* WT and W_DF, $\text{FADH}^\bullet \rightarrow \text{FAD}^{\text{ox}}$ occurs with a time constant of 12-13 min and $\text{FADH}^- \rightarrow \text{FADH}^\bullet$ with a time constant of 0.8-0.9 min. $\text{FADH}^\bullet \rightarrow \text{FAD}^{\text{ox}}$ in chicken and pigeon *Cry4* WT occurs with time constants of 29 min and 4 min respectively.

Comparison of light intensity used in re-oxidation experiments with the intensity of sunlight

The illuminance of surfaces subjected to full daylight (not direct sun) is in the range 10,000 to 25,000 lux. The corresponding figure for direct sunlight is $\sim 10^5 \text{ lux}^{78}$. The solar spectrum is approximately flat across the range of visible wavelengths⁷⁹. Therefore, on the basis that FAD^{ox} absorbs in the range 400-500 nm and the visible spectrum extends over 400-700 nm, *Cry4* should be capable of absorbing roughly a third of the total amount of visible sunlight. The intensity of indirect sunlight in the wavelength range where the FAD^{ox} state of *Cry4* absorbs is therefore 3,000 to 10,000 lux. The corresponding figure for direct sunlight is $\sim 30,000 \text{ lux}$.

The light intensities used in the re-oxidation measurements at 450 nm were $260 \mu\text{mol m}^{-2} \text{s}^{-1} \approx 70 \text{ W m}^{-2}$ (low power experiments) and $2600 \mu\text{mol m}^{-2} \text{s}^{-1} \approx 700 \text{ W m}^{-2}$ (high power experiments). To convert W m^{-2} to lux, one needs the photopic luminosity function for a bird's eye at 450 nm⁸⁰. For human eyes, the photopic luminosity at 450 nm is $\sim 5\%$ of that at the peak of the function, at 555 nm where $1 \text{ W m}^{-2} = 683 \text{ lux}^{78}$. Birds have better vision than humans at short wavelengths because they have UV cone photoreceptors: a rough estimate of a bird's luminosity function at 450 nm is 50% of that for humans at 555 nm. Therefore, for monochromatic light at 450 nm, $1 \text{ W m}^{-2} \approx 340 \text{ lux}$, giving 24,000 lux for the low power experiments and 240,000 for the high power experiments.

Therefore, the low power irradiation condition corresponds to approximately twice the intensity of bright indirect sunlight and the high power condition to ~ 7 times the intensity of direct sunlight. If the rate constants we have measured for purified *ErCry4* in isolation are similar to those *in vivo*, these experiments suggest that *ErCry4* in a bird's eye would be only partially photo-reduced even in broad daylight and would re-oxidise to the FAD^{ox} state in less than an hour. Considerably less photo-reduction might be expected at sunset when the solar illuminance is $\sim 400 \text{ lux}^{78}$.

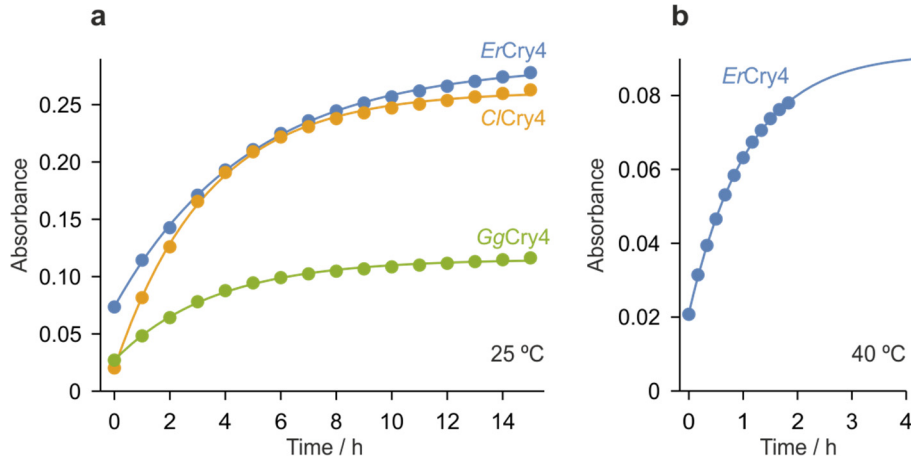


Fig. S18. Kinetics of re-oxidation of photo-reduced Cry4 WT proteins in the presence of 5 mM dithiothreitol (DTT).

(a) Time-dependence of the recovery of FAD^{ox} absorbance under aerobic conditions after 1-min illumination at 450 nm for *ErCry4* WT, *ClCry4* WT, and *GgCry4* WT at 25 °C.

(b) A similar measurement for *ErCry4* WT at 40 °C.

For (a), sixteen UV-vis spectra, recorded at intervals of 1.0 h, were each fitted to a model function of the form:

$$a(t)S_{\text{FAD}^{\text{ox}}}(\lambda) + b(t)S_{\text{FADH}}(\lambda) + c(t)S_{\text{FAD}^{\text{red}}}(\lambda) + d(t)\exp[-(\lambda/\text{nm}-330)/e(t)], \quad (\text{S.16})$$

where $S_{\text{FAD}^{\text{ox}}}(\lambda)$, $S_{\text{FADH}}(\lambda)$ and $S_{\text{FAD}^{\text{red}}}(\lambda)$ are the species-associated spectra shown in Fig. S17(c) and the final term is an empirical model of the scattering caused by small amounts of aggregated protein. λ is the wavelength in nm. The figure shows $a(t)$, the amplitude of the FAD^{ox} component, for robin, pigeon and chicken Cry4 WT proteins (dots) together with fits to the exponential function (lines):

$$a(t) = a_0 - a_1 \exp(-t/\tau). \quad (\text{S.17})$$

The values of the time constants, τ , are given in Table S6.

Experimental conditions: 20 μM protein in 20 mM Tris buffer, pH 8.0, 250 mM NaCl, 5 mM DTT, with 20% glycerol at 25 °C. Light intensity at 450 nm: 140 $\mu\text{mol m}^{-2} \text{s}^{-1}$. 1 min irradiation time.

For (b), twelve UV-vis spectra were recorded at intervals of 10 min and analysed as described for (a). Protein aggregation, manifested as a strong scattering signal, was much more pronounced than at 25 °C. The value of the time constant, τ , is given in Table S6. Note the different time axes for the two plots.

Experimental conditions: 10 μM protein in 20 mM Tris buffer, pH 8.0, 250 mM NaCl, 5 mM DTT, with 20% glycerol at 40 °C. Light intensity at 450 nm: 140 $\mu\text{mol m}^{-2} \text{s}^{-1}$. 1 min irradiation time.

Cry4	$T / ^\circ\text{C}$	τ / h	$t_{1/2} / \text{h}$
Robin	25	4.9	3.4
Pigeon	25	3.3	2.3
Chicken	25	3.6	2.5
Robin	40	1.1	0.8

Table S6. Time constants (τ) and half lives ($t_{1/2}$) obtained from the FAD^{ox} recovery data in Fig. S18 using Eqn (S.17).

The re-oxidation rate of photo-reduced the FAD^{ox} state of robin Cry4 is 4.5 times faster at 40 $^\circ\text{C}$ than at 25 $^\circ\text{C}$.

Comment on Cry4 re-oxidation kinetics

Slow re-oxidation of Cry4 proteins under strongly reducing conditions has been reported previously: Ozturk *et al.* (pigeon, zebrafish)⁸¹, Wang *et al.* (pigeon)⁸², Mitsui *et al.* (pigeon)⁸³, Zoltowski *et al.* (pigeon)¹⁵, Otsuka *et al.* (chicken)⁸⁴. We report here similar re-oxidation times for robin, chicken and pigeon Cry4s in the presence of 5mM DTT (Fig. S18 and Table S6) and much faster recovery in neutral redox conditions (Fig. S16 and Table S5). These differences agree with van Wilderen *et al.*⁸⁵ who found that $\text{FADH}^\bullet \rightarrow \text{FAD}^{\text{ox}}$ in *Arabidopsis thaliana* Cry1 is slower by more than an order of magnitude when measured in the presence of 3 mM DTT. Related differences have also been found for chicken Cry4⁸⁴.

Nothing is known about the distribution of the different redox species (GSH/GSSG, H_2O_2 , $\text{O}_2^{\bullet-}$, NO, NAD^+/NADH — all central to redox homeostasis and redox signalling) within different tissues and subcellular compartments in any migratory bird. In an attempt to establish a quantitative *in vivo* mapping in *Drosophila* larvae by using genetically encoded redox probes, Albrecht *et al.*⁸⁶ could show that physiological redox differences and changes can be seen in living larvae and that they are distinct in terms of location, tissue type, subcellular compartment, and redox chemistry. Since we know nothing about the *in vivo* redox state of the surrounding environment of Cry4 in retina cells, making data-founded statements about flavin re-oxidation *in vivo* in birds is therefore not possible.

However, we do know that intense physical activity and high metabolic activity are generally associated with increased production of reactive oxygen species (ROS). Thus ROS production rates are expected to be substantially higher in animals, particularly in birds, that show inherently high rates of oxygen consumption^{87,88}. Jenni-Eiermann⁸⁹ found, for example, that the European robin experiences oxidative damage during migratory flights. Migratory birds, much more than birds that do not migrate, are faced with the problem of overcoming these oxidative challenges posed by extreme flights and have a need to increase their antioxidant responses⁹⁰.

In conclusion, far too little is known about the redox conditions in robin retina cells to be able to say how relevant any of the *in vitro* measurements of *ErCry4* re-oxidation rates are to the situation *in vivo*. However, our *in vitro* results do at least show that there are conditions under which robin Cry4 is capable to being re-oxidised (presumably by O_2) in less than 1 h without added oxidants.

Magnetic field effects without added ferricyanide

In many of the experiments reported in the main text, potassium ferricyanide was added to the samples to speed up the recovery time of the photoreduced form of the protein and so reduce the time needed to acquire spectra with satisfactory signal-to-noise ratio. To check that there was no effect of this oxidant on the magnetic sensitivity, we repeated one of the CRDS measurements without added $\text{K}_3\text{Fe}(\text{CN})_3$.

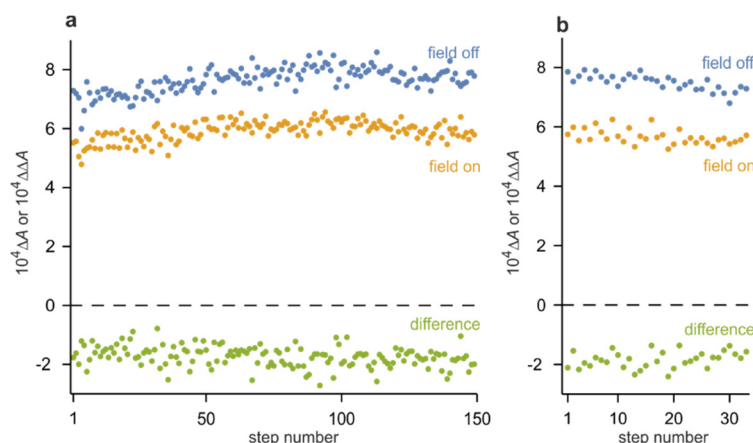


Fig. S19. Magnetic field effect on *ErCry4* W₆F mutant with/without added $\text{K}_3\text{Fe}(\text{CN})_3$.

(a) No $\text{K}_3\text{Fe}(\text{CN})_3$. CRDS signals from 150 consecutive measurements at 5-min intervals with (yellow) and without (blue) a 30 mT applied magnetic field, with a pump-probe delay of 2 μs . The difference signal, $\Delta \Delta A = \Delta A(\text{on}) - \Delta A(\text{off})$, is shown in green. The averages of these signals are given in [Table S7](#).

(b) 5 mM $\text{K}_3\text{Fe}(\text{CN})_3$. CRDS signals measured under the same conditions but with added Fe(III). 33 consecutive measurements at 1-min intervals.

Experimental conditions: 60 μM protein in 10 mM Tris buffer, pH 8.0, 250 mM NaCl, with 20% glycerol at 278 K.

5 mM Fe(III)		
	mean	s.d.
$\Delta A(\text{off})$	7.50×10^{-4}	0.26×10^{-4}
$\Delta A(\text{on})$	5.66×10^{-4}	0.25×10^{-4}
$\Delta\Delta A$	-1.84×10^{-4}	0.28×10^{-4}
MFE	-24.5%	3.7%

no Fe(III)		
	mean	s.d.
$\Delta A(\text{off})$	7.66×10^{-4}	0.42×10^{-4}
$\Delta A(\text{on})$	5.92×10^{-4}	0.33×10^{-4}
$\Delta\Delta A$	-1.74×10^{-4}	0.34×10^{-4}
MFE	-22.7%	4.5%

Table S7. Magnetic field effects on *ErCry4* W_DF mutant with/without added K₃Fe(CN)₃.

The means and standard deviations of the ΔA and $\Delta\Delta A$ signals at pH 8 were calculated from the measurements shown in [Fig. S19](#). Fe(III) has no effect on the magnetic sensitivity of *ErCry4* W_DF.

The magnetic field effect measured for *ErCry4* W_DF at pH 7 under otherwise identical conditions in the presence of 5 mM K₃Fe(CN)₃ was $-17.5\% \pm 1.0\%$ ([Fig. 2b](#)).

References

- 46 Lee, A. A. *et al.* Alternative radical pairs for cryptochrome-based magnetoreception. *J. R. Soc. Interface* **11**, 20131063 (2014).
- 47 Arnold, K., Bordoli, L., Kopp, J. & Schwede, T. The SWISS-MODEL workspace: a web-based environment for protein structure homology modelling. *Bioinformatics (Oxford, England)* **22**, 195-201 (2006).
- 48 Phillips, J. C. *et al.* Scalable molecular dynamics with NAMD. *J. Comput. Chem.* **26**, 1781-1802 (2005).
- 49 Korol, V. *et al.* Introducing VIKING: a novel online platform for multiscale modeling. *ACS Omega* **5**, 1254-1260 (2020).
- 50 Nielsen, C., Kattnig, D. R., Sjulstok, E., Hore, P. J. & Solov'yov, I. A. Ascorbic acid may not be involved in cryptochrome-based magnetoreception. *J R Soc Interface* **14**, 20170657 (2017).
- 51 Jepsen, K. A. & Solov'yov, I. A. On binding specificity of (6-4) photolyase to a T(6-4)T DNA photoproduct. *Eur. Phys. J. D* **71**, 155 (2017).
- 52 MacKerell, A. D. *et al.* All-atom empirical potential for molecular modeling and dynamics studies of proteins. *J. Phys. Chem. B* **102**, 3586-3616 (1998).
- 53 MacKerell, A. D., Feig, M. & Brooks, C. L. Extending the treatment of backbone energetics in protein force fields: Limitations of gas-phase quantum mechanics in reproducing protein conformational distributions in molecular dynamics simulations. *J. Comput. Chem.* **25**, 1400-1415 (2004).
- 54 Best, R. B. *et al.* Optimization of the additive CHARMM all-atom protein force field targeting improved sampling of the backbone ϕ , ψ and side-chain $\chi(1)$ and $\chi(2)$ dihedral angles. *J Chem Theory Comput* **8**, 3257-3273 (2012).
- 55 Solov'yov, I. A., Domratcheva, T., Shahi, A. R. M. & Schulten, K. Decrypting cryptochrome: revealing the molecular identity of the photoactivation reaction. *J. Am. Chem. Soc.* **134**, 18046-18052 (2012).
- 56 Lüdemann, G., Solov'yov, I. A., Kubar, T. & Elstner, M. Solvent driving force ensures fast formation of a persistent and well-separated radical pair in plant cryptochrome. *J. Am. Chem. Soc.* **137**, 1147-1156 (2015).
- 57 Solov'yov, I. A., Domratcheva, T. & Schulten, K. Separation of photo-induced radical pair in cryptochrome to a functionally critical distance. *Sci. Rep.* **4**, 3845 (2014).
- 58 Sjulstok, E., Solov'yov, I. A. & Freddolino, P. L. in *New Approaches for Flavin Catalysis* Vol. 620 (ed Bruce A. Palfey) 277-314 (2019).
- 59 Feller, S. E., Zhang, Y. H., Pastor, R. W. & Brooks, B. R. Constant-pressure molecular-dynamics simulation - the Langevin piston method. *J. Chem. Phys.* **103**, 4613-4621 (1995).
- 60 Darden, T., York, D. & Pedersen, L. Particle mesh Ewald: An $N \cdot \log(N)$ method for Ewald sums in large systems. *J. Chem. Phys.* **98**, 10089-10092 (1993).
- 61 Humphrey, W., Dalke, A. & Schulten, K. VMD: Visual molecular dynamics. *J. Mol. Graphics* **14**, 33-38 (1996).
- 62 Yanai, T., Tew, D. P. & Handy, N. C. A new hybrid exchange–correlation functional using the Coulomb-attenuating method (CAM-B3LYP). *Chem. Phys. Lett.* **393**, 51-57 (2004).
- 63 Frisch M.J. *et al.* Gaussian 09, Revision D.01 (Gaussian, Inc., Wallingford, CT, USA, 2013).
- 64 Miyashita, O., Okamura, M. Y. & Onuchic, J. N. Theoretical understanding of the interprotein electron transfer between cytochrome c2 and the photosynthetic reaction center. *J. Phys. Chem. B* **107**, 1230-1241 (2003).
- 65 King, G. & Warshel, A. Investigation of the free energy functions for electron transfer reactions. *J. Chem. Phys.* **93**, 8682-8692 (1990).
- 66 Parson, W. W., Chu, Z. T. & Warshel, A. Reorganization energy of the initial electron-transfer step in photosynthetic bacterial reaction centers. *Biophys. J.* **74**, 182-191 (1998).

- 67 Cailliez, F., Müller, P., Firmino, T., Pernot, P. & de la Lande, A. Energetics of photoinduced charge migration within the tryptophan tetrad of an animal (6–4) photolyase. *J. Am. Chem. Soc.* **138**, 1904–1915 (2016).
- 68 Moser, C. C., Anderson, J. L. R. & Dutton, P. L. Guidelines for tunneling in enzymes. *Biochim. Biophys. Acta Bioenerg.* **1797**, 1573–1586 (2010).
- 69 Page, C. C., Moser, C. C., Chen, X. & Dutton, P. L. Natural engineering principles of electron tunnelling in biological oxidation-reduction. *Nature* **402**, 47–52 (1999).
- 70 Balabin, I. A., Hu, X. & Beratan, D. N. Exploring biological electron transfer pathway dynamics with the Pathways Plugin for VMD. *J. Comput. Chem.* **33**, 906–910 (2012).
- 71 Prytkova, T. R., Kurnikov, I. V. & Beratan, D. N. Coupling Coherence Distinguishes Structure Sensitivity in Protein Electron Transfer. *Science* **315**, 622–625 (2007).
- 72 Liu, B., Liu, H., Zhong, D. & Lin, C. Searching for a photocycle of the cryptochrome photoreceptors. *Curr. Opin. Plant Biol.* **13**, 578–586 (2010).
- 73 Langenbacher, T., Immeln, D., Dick, B. & Kottke, T. Microsecond Light-induced Proton Transfer to Flavin in the Blue Light Sensor Plant Cryptochrome. *Journal of the American Chemical Society* **131**, 14274–14280 (2009).
- 74 Santabarbara, S. *et al.* Bidirectional electron transfer in photosystem I: Determination of two distances between P(700)(+) and A(1)(-) in spin-correlated radical pairs. *Biochemistry* **44**, 2119–2128 (2005).
- 75 van Wilderen, L. J. G. W., Lincoln, C. N. & van Thor, J. J. Modelling multi-pulse population dynamics from ultrafast spectroscopy. *Plos One* **6**, e17373 (2011).
- 76 Nagai, H., Kuwabara, K. & Carta, G. Temperature dependence of the dissociation constants of several amino acids. *J. Chem. Engin. Data* **53**, 619–627 (2008).
- 77 Muller, P., Ignatz, E., Kiontke, S., Brettel, K. & Essen, L. O. Sub-nanosecond tryptophan radical deprotonation mediated by a protein-bound water cluster in class II DNA photolyases. *Chem. Sci.* **9**, 1200–1212 (2018).
- 78 <https://en.wikipedia.org/wiki/Lux>.
- 79 <https://en.wikipedia.org/wiki/Sunlight>.
- 80 https://en.wikipedia.org/wiki/Luminosity_function.
- 81 Ozturk, N. *et al.* Comparative photochemistry of animal Type 1 and Type 4 cryptochromes. *Biochemistry* **48**, 8585–8593 (2009).
- 82 Wang, X. *et al.* Comparative properties and functions of type 2 and type 4 pigeon cryptochromes. *Cell. Molec. Life Sci.* **75**, 4629–4641 (2018).
- 83 Mitsui, H. *et al.* Overexpression in yeast, photocycle, and in vitro structural change of an avian putative magnetoreceptor cryptochrome 4. *Biochemistry* **54**, 1908–1917 (2015).
- 84 Otsuka, H. *et al.* Rapid oxidation following photoreduction in the avian cryptochrome 4 photocycle. *Biochemistry* **59**, 3615–3625 (2020).
- 85 van Wilderen, L. J. G. W., Silkstone, G., Mason, M., van Thor, J. J. & Wilson, M. T. Kinetic studies on the oxidation of semiquinone and hydroquinone forms of *Arabidopsis* cryptochrome by molecular oxygen. *Febs Open Bio* **5**, 885–892 (2015).
- 86 Albrecht, S. C., Barata, A. G., Grosshans, J., Teleman, A. A. & Dick, T. P. In vivo mapping of hydrogen peroxide and oxidized glutathione reveals chemical and regional specificity of redox homeostasis. *Cell Metab* **14**, 819–829 (2011).
- 87 Skrip, M. M. & McWilliams, S. R. Oxidative balance in birds: an atoms-to-organisms-to-ecology primer for ornithologists. *J. Field Ornithol.* **87**, 1–20 (2016).
- 88 Costantini, D. Oxidative stress in ecology and evolution: lessons from avian studies. *Ecol. Lett.* **11**, 1238–1251 (2008).
- 89 Jenni-Eiermann, S., Jenni, L., Smith, S. & Costantini, D. Oxidative stress in endurance flight: An unconsidered factor in bird migration. *Plos One* **9**, 1–6 (2014).
- 90 Gutierrez, J. S. *et al.* Oxidative status and metabolic profile in a long-lived bird preparing for extreme endurance migration. *Sci. Rep.* **9**, 17616 (2019).